Dentate spikes and external control of hippocampal function

Dvorak, D.[1], Chung, A.[1,*], Park E. H.[1], Fenton, A. A.[1,2,3]

[1] Center for Neural Science, New York University, New York, NY

[2] Neuroscience Institute at the NYU Langone Medical Center, New York, NY

[3] The Robert F. Furchgott Center for Neural and Behavioral Science, Dept. of Physiology and Pharmacology, SUNY, Downstate Medical Center, Brooklyn, NY

[*] Massachusetts General Hospital, Boston, MA (current affiliation)

Author for Correspondence:

André Fenton

Center for Neural Science and Neuroscience Institute at the NYU Langone Medical Center

(212) 992 6573

afenton@nyu.edu

Abstract

Mouse hippocampus CA1 place-cell discharge typically encodes current location but during slow gamma dominance (SG_{dom}), when slow gamma oscillations (30-50 Hz) dominate mid-frequency gamma oscillations (70-90 Hz) in CA1 local field potentials, CA1 discharge switches to represent distant recollected locations. We report that dentate spike type 2 (DS_M) events initiated by MECII→DG inputs promote SG_{dom} and change excitation-inhibition coordinated discharge in DG, CA3, and CA1, whereas type 1 (DS_L) events initiated by LECII→DG inputs do not. Just before SG_{dom}, LECII-originating slow gamma oscillations in dentate gyrus and CA3-originating slow gamma oscillations in CA1 phase and frequency synchronize at the DS_M peak when discharge within DG, CA3, and CA1 increases to promote excitation-inhibition cofiring within and across the DG→CA3→CA1 pathway, optimizing discharge for the 5-10 ms DG-to-CA1 neuro-transmission that coincides with SG_{dom}. Several DS_M properties identify extrahippocampal control of SG_{dom}, and a cortico-hippocampal mechanism that switches between memory-related information processing modes.

Introduction

The hippocampus is critical for long-term memory storage and use, requiring that neural discharge represent both what has occurred and what is happening. How do multifunction neural networks like hippocampus accomplish mutually incompatible tasks like recollecting the past and encoding the present? One possibility is that separate neural circuits operate in parallel to perform each information processing task, but this does not appear to be the case for hippocampus. Rather, in hippocampus the same populations of excitatory and inhibitory neurons are organized such that network discharge patterns, sometimes called cell assemblies (Harris et al., 2003; Hebb, 1949) rapidly switch between different information processing modes, often in a winner-take-all fashion during vicarious-trial-and-error and other choice behaviors (Colgin, 2015; Kelemen and Fenton, 2010; Kelemen and Fenton, 2013; Kelemen and Fenton, 2016; Papale et al., 2016; Pastalkova et al., 2008; van Dijk and Fenton, 2018; Wu et al., 2017). Indeed, we first reported variability in the discharge of hippocampus place cells that was so extreme it was incompatible with these cells merely signaling the current location within a single cognitive map (Fenton and Muller, 1998; Jackson and Redish, 2007; Olypher et al., 2002a, b) and we and others went on to show that this variability could be explained as multiple spatial representations during tasks with purposeful behaviors that were directed to specific places (Fenton et al., 2010; Kelemen and Fenton, 2010; Kelemen and Fenton, 2013; Kelemen and Fenton, 2016). It was recently reported that in an alternation task, such variability, organized as place representations that alternate within sequences of ~8 Hz theta oscillations, perhaps reflecting planning between which upcoming alternatives to choose (Kay et al., 2020). We previously reported that position-representing CA1 ensemble spike trains switch between representing the current, local position and distant specific places, which during an active place avoidance task represented recollected locations of prior foot-shock (Dvorak et al., 2018). We observed that CA1 discharge switched to signaling distant places during slow-gamma

dominance (SG_{dom}), when CA1 slow gamma (30-50 Hz) oscillations dominate CA1 mid-frequency (70-90 Hz) gamma oscillations (Dvorak et al., 2018). Now that it is established that such network transitions occur to change hippocampal cognitive information processing, it is essential to understand how such transitions might occur in hippocampus as well as other cognitive networks that transiently switch information processing modes in circumstances that are physically unchanged. Here we present single cell ensemble discharge evidence of the switching between encoding local positions and distant, recollected positions in CA1 discharge during the active place avoidance task (Dvorak et al., 2018) and then our discovery that a dentate spike event (Bragin et al., 1995) is a neural network mechanism of this switching.

Results

Slow gamma dominance in the CA1 LFP switches CA1 place discharge to recollection of distant locations

Well-trained mice on the rotating place avoidance arena make evasive movements away from the advancing shock zone as illustrated in the upper portion of Figure 1A. This avoidance behavior demonstrates the mice recollect locations where they were previously shocked. Approximately 2 seconds before running away to avoid the location of shock, we observe slow gamma dominance in the CA1 LFP, that is the result of a relatively increased rate of slow gamma (30-50 Hz) oscillations and a decreased rate of mid-frequency gamma (70-90 Hz) oscillations (Fig. 1A, lower). On average, the likelihood of SG_{dom} is elevated for several seconds before mice express the active avoidance, with the peak at 1.5 s before, during a period when the mouse is essentially inactive (Fig. 1A, B). In contrast, SG_{dom} is unlikely during the passive approach to the shock zone if the mouse will fail to avoid the approaching shock zone and rather runs away to escape after receiving a shock (Fig. 1B). Such failed avoidances are rare, and most likely occur because the mouse did not recollect the location of shock. Decoding the location being represented in the concurrent transient 500-ms discharge of place cell ensembles

indicate that place cells with firing fields at the location of shock discharge during SG_{dom} even though the mouse is at locations distant from the shock zone, which can be seen in both a single 5-s example (Fig. 1C) as well as in the group data (Fig. 1D). Conversely, place cell ensemble discharge continues to decode to the current location when mice fail to avoid shock (Dvorak et al., 2018). The fact that CA1 ensemble discharge can transiently switch from signaling current location to a distant, recollected location motivates us to ask, what network mechanism can cause this switch between information processing modes (Fig. 1E)?

One way to switch between multiple mutually-exclusive tasks is to organize the network such that its intrinsic excitation-inhibition dynamics are so balanced that the network spontaneously transitions between multiple information processing modes through intrinsic winner-take-all mechanisms (Fig. 1E, F upper; de Almeida et al., 2009; Rolls and Treves, 1998). Alternatively, an external control signal can select the information processing mode (Fig. 1F lower). In the extrinsic control case, distinct control input signals predict the transition into functional states. We previously reported that transient recollection-associated SG_{dom} events (Figs. 1A-D) occur at the same rate during free exploration or during the active place avoidance memory task (Dvorak et al., 2018), pointing to the possibility that SG_{dom} is unrelated to cognitive demand or environmental variables, and is instead the result of internal hippocampus dynamics (Fig. 1F upper; Kay et al., 2020; Stella et al., 2019).

Here we investigate an alternative, that these SG_{dom}-associated switches of the CA1 information processing mode are controlled by discrete events in the perforant path tri-synaptic input from the entorhinal cortex (Fig. 1F, lower).

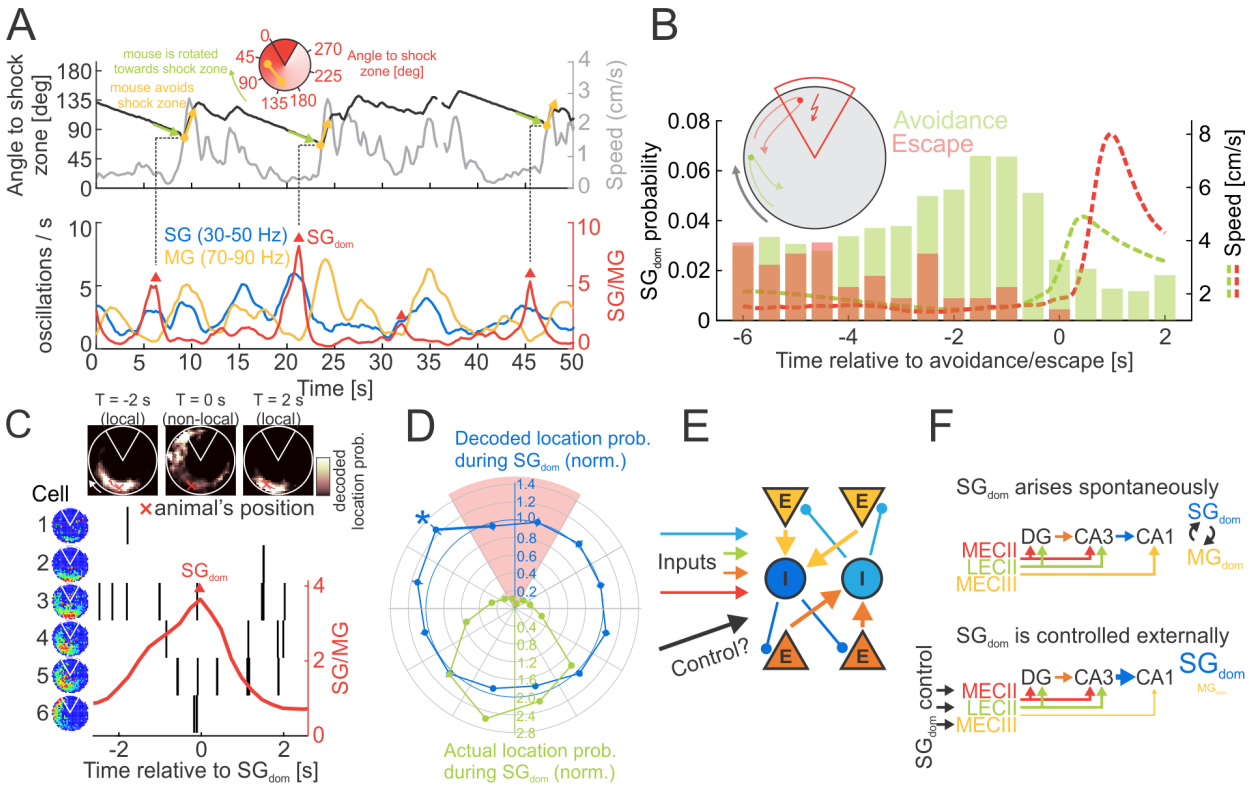

Figure 1. SG_{dom} is a biomarker of memory recollection. A) Avoidances (yellow vectors) mark evasive movements away from the shock zone without receiving shock. They are detected as local minima in the angle to the leading edge of the shock zone (black line) with preceding stillness (green vector) as the mouse is passively carried towards the shock zone by the rotating arena. Notice the abrupt speed (gray line) increases as the mouse accelerates away from the shock zone. SG_{dom} events are detected as local maxima (red triangles) in the ratio (red line) of rates of CA1 slow (blue; 30-50 Hz) and mid-frequency (yellow; 70-90 Hz) gamma oscillations. Notice that many SG_{dom} events precede avoidance movements by ~ 2 seconds. B) Probability histogram of SG_{dom} before avoidance (green; success = no shock received) and escape (red; failure = shock received). The corresponding speed profiles are shown as dashed lines. C) CA1 single unit discharge (vertical black lines) of a 6-cell ensemble during a 5 second time segment centered at SG_{dom} (red triangle). The firing rate map of each cell is shown on the left. The 2-D posterior probability distributions computed using Bayesian decoding (Dvorak et al., 2018;

Zhang et al., 1998) are shown at the top overlayed with the mouse's track during 5 seconds (red line) and its current location (red cross). Notice that the decoding of discharge is non-local during SG_{dom}. The otherwise accurate Bayesian posterior decodes to the shock zone, away from animal's current location. D) Normalized circular probability distribution of observed mouse locations during SG_{dom} (green) and normalized circular probability distribution of the decoded location (i.e., where decoding points to) during SG_{dom} (blue). The asterisk marks a significant deviation from 1 ($t_{778} = 3.10$, $p = 0.002$, corrected using Bonferroni's method; normalized using non-SG_{dom} events). Notice that SG_{dom} is predominant in the quadrant opposite to the shock zone, while SG_{dom} decodes to locations adjacent to the shock zone. E) A network schematic with winner-take-all dynamics, composed of excitatory (E) and inhibitory (I) neurons, excitatory inputs and a possible external control signal. F) Two hypotheses for hippocampal information processing control (upper) intrinsic, intrahippocampal and (lower) extrinsic, extrahippocampal control. Data in B and D from 2 mice.

Identifying the two types of dentate spike originating from distinct perforant path inputs

CA1 slow gamma originates in CA3 (Lasztoczi and Klausberger, 2014, 2016; Schomburg et al., 2014), motivating us to seek evidence of extrahippocampal control signals either directly via the temporoammonic input from entorhinal cortex layer 3 (ECIII) or indirectly from ECII via the perforant path to dentate gyrus (DG). We examine dentate spikes (DS), the under-investigated, large amplitude, short duration field potentials that localize to DG (Fig. 2A; Fig. S1A). They result from entorhinal activation; dentate spikes disappear after bilateral removal of entorhinal cortex (Bragin et al., 1995), and are thought to cause a synchronized inhibition of granule cells and downstream CA3 and CA1 networks (Fig. 2A left; Penttonen et al., 1997), therefore providing an ideal candidate for extrinsic control of hippocampal function. Two types of dentate spikes were previously identified in rat (Bragin et al., 1995) and mouse (Buzsaki et al., 2003). DS type 1 (DS_L in this study) exhibits a polarity reversal in the outer third of the DG molecular

layer at the termination zone of the lateral entorhinal cortex layer 2 (LECII) projection, whereas DS type 2 (DS_M in this study) exhibits a polarity reversal in the middle third of the DG molecular layer at the termination zone of the medial entorhinal cortex layer 2 (MECII) projection (Bragin et al., 1995). Similar to sharp-wave ripples (SWR), dentate spikes are synchronized across hemispheres (Bragin et al., 1995; Headley et al., 2017). If DS are related to recollection, like SG_{dom} (Dvorak et al., 2018), they should be related to behavior, but little is known about this relationship. Motivated by the distinctive connectivity underlying the two types of DS (Fig. 2A), the differential roles of LEC in non-spatial information and MEC in spatial information processing (Hargreaves et al., 2005; Knierim et al., 2014), and the limited information about DS events, we examine whether DS_L and/or DS_M can act as external control signals, switching CA1 into the SG_{dom}-associated mode of memory recollection.

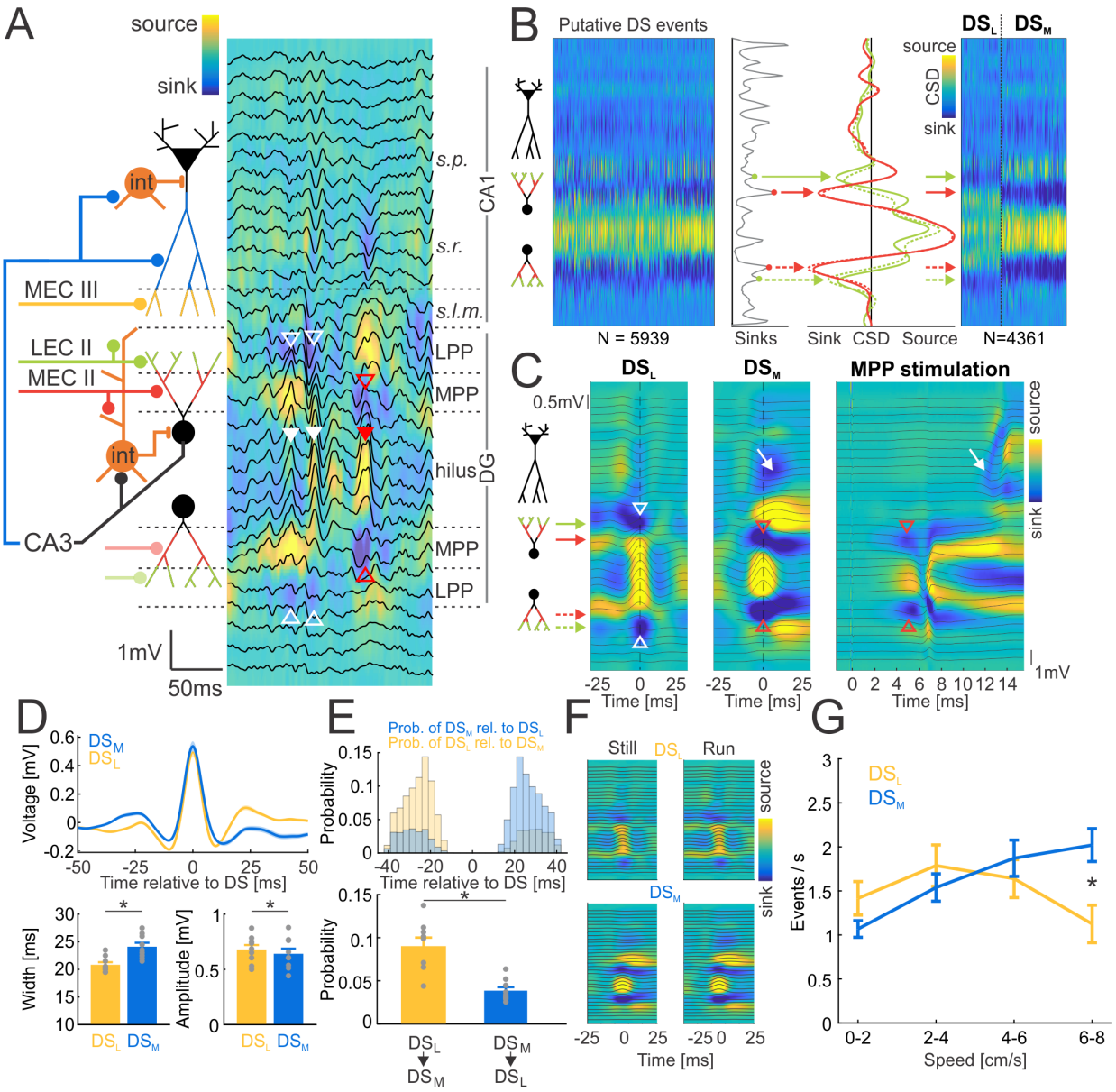

Figure 2. CSD analysis classifies two types of dentate spikes with distinct anatomical, temporal, and behavioral properties. A) Two types of dentate spikes can be identified in the LFP recorded from DG hilus. DS_L (full white arrowheads) is identified by a pair of current-source-density (CSD) sinks in the outer molecular layers of DG (empty white arrowheads) at the LECII projection termination. DS_M (full red arrowheads) is identified by a pair of CSD sinks in the middle molecular layers of DG (empty red arrowheads) at the MECII projection termination. Background color represents CSD. Black traces represent LFP. Simplified circuit schematics

(left) illustrating hypothesized components of dentate spike generation and mechanism of CA1 SG_{dom} control. B) CSD of putative DS events (left) shows pairs of sink bands at the outer and middle molecular layers of DG. Histogram of local minima in CSD profiles (middle) shows peaks aligned with pairs of sink bands in the outer and middle molecular layers. Average CSD profiles (right) of the two types of DS events with CSD minima in the vicinity of the peaks of the CSD minima histograms. Notice the correspondence at the outer molecular layers (solid green and dashed green traces) and at the middle molecular layers of DG (solid red and dashed red traces) pointing to the symmetry of the DS-associated CSD sinks. C) Average CSDs of DS_L (left) and DS_M (middle). Notice sinks in outer molecular layers (white empty arrowheads) for DS_L and middle molecular layers (red empty arrowheads) for DS_M. The CSD of the evoked response to medial perforant path (MPP) stimulation (right), evokes sinks (red empty arrowheads) at the same locations of the DS_M sinks. A ~6 ms latency sink at CA1 *stratum radiatum* occurs after both the MPP evoked response and DS_M (white arrow), but not after DS_L. D) Average LFP of DS_L (yellow) and DS_M (blue) with their width and amplitude comparisons (bottom). E) Histograms illustrate that DS_M often follows DS_L (top) and the probability of observing $DS_L \rightarrow DS_M$ vs. $DS_M \rightarrow DS_L$ pairs (bottom). F) Average CSDs of DS_L (top) and DS_M (bottom) during stillness (speed < 2 cm/s; left) and running (speed > 3 cm/s; right). G) Relationship between DS rates and the mouse's speed. Averages ± S.E.M. are plotted.

Identifying DS_L and DS_M events using current source density analysis

We begin by assuming that the two types of dentate spikes can have different functional roles, which requires distinguishing DS_L and DS_M events in the LFPs that we record across the somato-dendritic CA1-DG axis (Fig. 2A; Fig. S1). Putative DS events localize to the dentate hilus. When current source density (CSD) profiles are computed at the DS event peaks, pairs of current sinks localize at both the suprapyramidal and infrapyramidal molecular layers of DG (Fig. 2A, left; Bragin et al., 1995). We then identify local minima in the CSD profiles of each

putative DS event and compute the histogram along the dorso-ventral axis (Fig. 2B, middle; Star Methods), which reveals a peak concentration of CSD sinks aligned with the visually identified sink regions that correspond to the molecular layers of DG. Putative DS events are classified according to the location of the current sink within the sink histogram. DS_L (DS type 1) sinks are at the outer molecular layers of DG where LECII projections terminate. DS_M (DS type 2) sinks are at the middle molecular layers of DG, where MECII projections terminate. When we average the CSDs of DS_L and DS_M events separately for classification according to either the suprapyramidal (solid lines in Fig. 2B, right) or the infrapyramidal (dashed lines in Fig. 2B, right) molecular layers, both types of classifications result in events with the same CSD profile. Consequently, we use DS classification according to the presence or absence of a sink at the suprapyramidal molecular layer.

We confirm localization of the outer and middle molecular layers of DG, by electrically stimulating the medial perforant path (MPP) and computing the average CSD of the evoked response (Fig. 2C, right). The evoked response matches the average CSD of DS_M (Fig. 2C, middle), but not DS_L events (Fig. 2C, left), as expected. DS_M (Fig. 2C, middle; T = 0 ms) and evoked responses (Fig. 2C, right; T = 5 ms) have colocalized pairs of current sinks (red empty arrowheads in Fig. 2C) in the middle molecular layers of DG, whereas the DS_L sinks are in the outer molecular layers (white empty arrowheads in Fig. 2C). We are thus confident in identifying distinct DS_L and DS_M events, an advance over prior work.

DS_M events often follow DS_L events

Comparing DS_L and DS_M events (Fig. 2D), the DS_M width is greater than DS_L (paired $t_8 = 8.56$, $p = 10^{-5}$) while DS_L amplitude is larger than DS_M (paired $t_8 = 2.87$, $p = 0.02$). DS_M has a higher shoulder ~25 ms before the peak, and DS_L has a higher shoulder about ~25 ms after the peak. The probability of observing DS_L before DS_M is greater than the probability of observing DS_M

before DS_L (Fig. 2E; paired $t_8 = 5.61$, $p = 10^{-4}$). The average CSDs of DS_L and DS_M during stillness (speed < 2 cm/s) and running (speed > 3 cm/s) do not visibly differ (Fig. 2F). Rates of DS_L and DS_M events are not different, but both types of DS are differentially modulated by speed. DS_M rates increase linearly with speed, whereas DS_L do not (Fig. 2G; 2-way type x speed $ANOVA_{r.m.}$, type: $F_{1,14} = 0.02$, $p = 0.88$; speed: $F_{3,12} = 5.53$, $p = 0.013$; interaction: $F_{3,12} = 5.26$, $p = 0.015$, post-hoc tests: $DS_M > DS_L$ at the greatest speeds of 6-8 cm/s). Thus, DS_L and DS_M are distinct in origin and morphology but not independent, are modulated by behavior, and DS_M is more likely to follow DS_L.

Dentate spikes modulate oscillatory activity in CA1

We investigate whether DS_L and DS_M influence the CA1 oscillatory activity components of SG_{dom}. Computing the event-triggered wavelet spectrum averages centered at each type of dentate spike shows that the wavelet spectrum is contaminated by the spectral leakage of DS events in the 30-50 Hz range, preventing analysis of CA1 oscillatory dynamics using LFP spectral power (Fig. 3A). Accordingly, we use independent component analysis (ICA; Star Methods), which identifies two independent components (IC) in the CA1 LFP below 100 Hz (Fig. 3B), a *stratum radiatum*-localized slow gamma IC (SG_{sr} ; mean frequency 34.1 ± 3.0 Hz; Fig. 3C, left; Fig. S2A) and a *lacunosum moleculare*-localized mid-frequency gamma IC (MG_{slm}; mean frequency 68.9 ± 3.4 Hz; Fig. 3C, right; Fig. S2A).

If dentate spikes modulate CA1 oscillatory activity, they should systematically co-occur with SG_{sr} and MG_{slm} oscillatory events. We use the phase of CA1 *stratum pyramidale* theta (6-12 Hz) as a common reference time and extract the phases of DS peaks and the phases of oscillatory events as local peaks in the z-score normalized wavelet spectrograms within 25-45 Hz for SG_{sr} and 45-85 Hz for MG_{slm}. In agreement with other studies (Fernandez-Ruiz et al., 2017; Lasztoczi and Klausberger, 2014) SG_{sr} oscillatory events occur close to the theta trough (339.2° ± 71.4°),

whereas the MG_{slm} oscillatory events occur close to the theta peak (220.5° ± 59.9°; Fig. 3D top). DS_M events occurred at the theta trough, coinciding with SG_{sr} oscillatory events (344.0° ± 59.8; Watson-Williams multi-sample test $F_{1,15} = 0.19$, $p = 0.67$), whereas the DS_L events occurred close to the theta peak, coinciding with the MG_{slm} oscillatory events (233.6° ± 71.2°; Watson-Williams multi-sample test $F_{1,15} = 3.48$, $p = 0.08$; Fig. 3D).

The theta phase alignment of DS_L and MG_{slm} events and the distinct phase alignment of DS_M and SG_{sr} events might be expected if DS events control CA1 gamma events, motivating us to determine whether DS events also influence locally-generated CA1 gamma power. We compute DS_L- and DS_M-triggered IC power profiles by averaging the z-scored wavelet spectrogram across 25-45 Hz for SG_{sr} and 45-85 Hz for MG_{slm} (Fig. 3E). To evaluate if the potential influence of the DS events on the CA1 ICs is distinct from the theta modulation of IC power (see Fig. 3D), we also compute control power profiles triggered by random events that were sampled from the DS_L and DS_M theta phase distributions. Accordingly, the random profiles that have the same theta phase distribution as the corresponding DS events, but only a chance association with the DS events are used for statistical comparisons. Data from 8 of 9 mice are analyzed because one mouse did not have CA1 electrode coverage. The MG_{slm} is strongly (36 %) increased at the DS_L peak compared to random (paired $t_7 = 6.82$, $p = 10^{-4}$), while the SG_{sr} is not (paired $t_7 = 0.35$, $p = 0.7$; Fig. 3E, left). In contrast, the SG_{sr} is strongly (67 %) increased at the peak of DS_M compared to random (paired $t_7 = 5.0$, $p = 0.002$), while the MG_{slm} is decreasing during DS_M (paired $t_7 = 2.68$, $p = 0.03$; Fig. 3E, right). Thus, the two DS events differentially modulate the SG_{sr} and MG_{slm} oscillations in CA1.

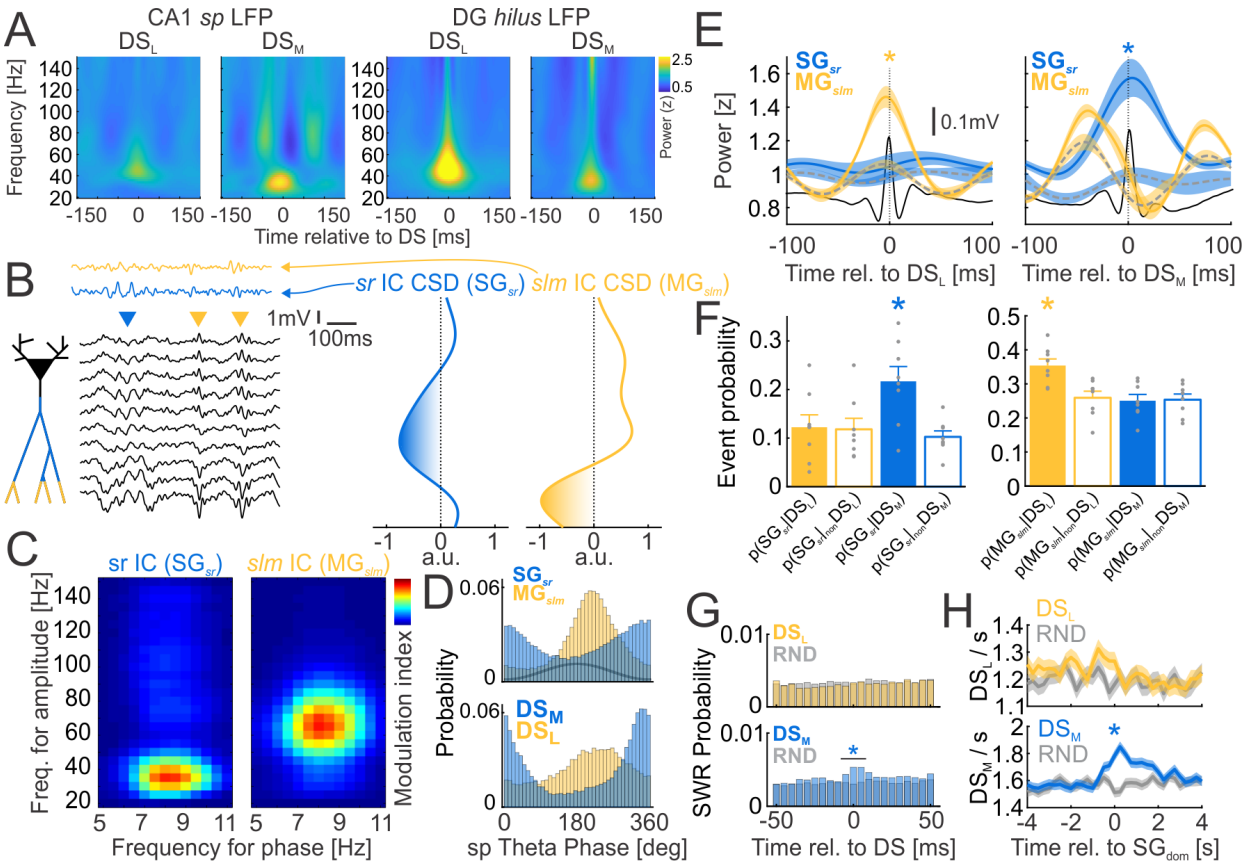

Figure 3. Dentate spikes modulate SG_{dom} and gamma oscillatory activity and in CA1 A) Average wavelet spectrogram of CA1 *stratum pyramidale* LFP (left) and DG hilar LFP (right), triggered by DS_L and DS_M events reveals non-specific patterns of activity defined by volume-conducted potentials associated with the DS spectral leakage in the 30-50 Hz range. Notice that the peak frequency of the DS-associated spectral leakage is higher in the narrower DS_L events and lower in the wider DS_M events as expected (compare with Fig. 2D). B) ICA decomposition of CA1 LFPs identifies two independent components (IC) < 100 Hz that correspond to *stratum radiatum* dendritic input (SG_{sr}, CA1 slow gamma, blue), and *stratum lacunosum moleculare* dendritic input (MG_{slm}, CA1 mid-frequency gamma, yellow). Arrowheads mark SG_{sr} (blue) and MG_{slm} (yellow) oscillatory events in this example LFP. The CSDs of ICA voltage loadings (right) show a SG_{sr} sink in *stratum radiatum* and a MG_{slm} sink in *stratum lacunosum moleculare*. C) Comodulograms between the phase of CA1 *stratum pyramidale* theta (5-11 Hz) and the SG_{sr}

and MG_{slm} gamma amplitudes in the 20-150 Hz frequency range show frequency peaks in the slow gamma band for SG_{sr} and mid-frequency gamma band for MG_{slm}. D) Theta phase (black line) distribution of SG_{sr} (blue) and MG_{slm} (yellow) oscillatory events (top) compared to theta phase distribution of DS_M (blue) and DS_L (yellow) events (bottom). E) Power averages of SG_{sr} (blue) and MG_{slm} (yellow) centered on DS_L (left) and DS_M (right). T=0 marks the DS peak. Profiles with gray dashed lines show IC power profiles at random times sampled from the same theta phase distributions as the corresponding DS_L and DS_M events. Black lines are DS_L and DS_M event averages. F) Coincidence of the DS and IC oscillatory events detected from SG_{sr} (left) and MG_{slm} (right) at random times. G) SWR probability distribution relative to the timing of DS_L (top) and DS_M (bottom) and random times (gray) during stillness. H) Rates of DS_L (top) and DS_M (bottom) centered at SG_{dom} (color) and randomly selected times (gray). Averages ± S.E.M. are plotted.

We next examine the co-occurrence of the DS and the CA1 gamma oscillatory events. We pick 1000 random times from each 30-min recording and assess whether an oscillatory event in the CA1 MG_{slm} or SG_{sr} occurs within a 50-ms coincidence interval of DS_L or DS_M. The probability of observing SG_{sr} is greater if DS_M is observed [Fig. 3F, left; ANOVA $F_{3,31} = 9.59$, $p = 10^{-4}$, $p(SG_{sr} \mid DS_M) > p(SG_{sr} \mid DS_L) = p(SG_{sr} \mid nonDS_M) = p(SG_{sr} \mid nonDS_L)$] while the probability of observing MG_{slm} is greater if a DS_L event is observed [Fig. 3F, right; ANOVA $F_{3,31} = 7.31$, $p = 10^{-4}$, $p(MG_{slm} \mid DS_L) > p(MG_{slm} \mid DS_M) = p(MG_{slm} \mid nonDS_L) = p(MG_{slm} \mid nonDS_M)$].

Since DS_M increases the power of CA3-originating SG_{sr} (Fig. 3E) and dentate spikes have been reported to co-occur with CA3-originating sharp wave ripples (SWR; Bragin et al., 1995), we next computed the probability of a SWR within ±50 ms of DS_L, DS_M, and random events during stillness (speed < 2 cm/s; Fig. 3G). SWR probability was increased in the vicinity of the DS_M peak but not DS_L (Fig. 3G; One sample test for proportions in the 20 ms window centered on

DS/RND events; p(SWR, DS_L) = 0.012, z = -0.71, p = 0.3; p(SWR, DS_M) = 0.018, z = 13.20, p = 10^{-39}).

Within the hypothesis that DS events control CA1 information processing mode, these findings of DS modulation of CA1 gamma predict that DS_M (but not DS_L) promotes SG_{dom} in CA1. Consequently, we evaluated this hypothesis using SG_{dom} events collected during place avoidance training, where SG_{dom} events identify memory recollection (Fig. 1). The rate of DS_M but not DS_L events is elevated at the time of SG_{dom} (DS_L: t_{5255} = 1.81, p = 0.07; DS_M: t_{5255} = 5.07, p < 0.0001).

Dentate spikes modulate individual cycles of CA1 gamma oscillations with millisecond precision, DS_M promoting SG_{dom}

If DS_M events control CA1 information processing by promoting SG_{dom}, then DS_M should influence CA1 gamma oscillations with a precision comparable to the ~7 ms conduction time from dentate gyrus to CA1 (Fig. 2C, white arrows). Because oscillatory power can only be studied at relatively long timescales, which corresponds to 3-5 cycles of an oscillatory burst or 100 ms in case of CA1 SG_{sr} oscillations (Figs. 3E, S2C), we developed a new method to analyze individual oscillatory cycles within each oscillatory burst (Star Methods). Because maximum spiking and therefore maximal information transfer appears during oscillatory minima (Fig. S2B; Dvorak and Fenton, 2014; Lasztoczi and Klausberger, 2016; Schomburg et al., 2012), we use the local minima of oscillatory bursts (red arrowheads in Fig. 4A inset) as discrete oscillatory events. This leads to a 7-fold improvement in time resolution (100ms for an entire oscillatory burst vs 15 ms for a half period of a single oscillatory cycle of SG_{sr}), a time scale that is comparable to the DG→CA1 transmission time (Fig. S2C). The probability of observing a MG_{slm} oscillatory cycle is strongly enhanced during the peak of DS_L (20-ms window centered on DS_L versus chance: paired t_7 = 5.43, p = 0.001; Fig 4A, left) as well as 15 ms before and 16 ms

after the DS_L peak, corresponding to a MG_{slm} oscillatory frequency of 69 Hz, whereas the probability of observing a SG_{sr} oscillatory cycle remains unchanged during DS_L (20-ms window centered on DS_L versus chance: paired $t_7 = 0.69$, $p = 0.52$; Fig 4A, left). In contrast, the probability of observing a SG_{sr} oscillatory cycle is enhanced 6 ms after the peak of DS_M, corresponding to the transmission time between DG and CA1, which is primarily influenced by the CA3→CA1 synaptic delay (Mizuseki et al., 2012; 20-ms window centered on DS_M versus chance: paired $t_7 = 4.52$, $p = 0.003$; Fig 4A, right). The probability of a SG_{sr} oscillatory cycle is also enhanced 24 ms before and 33 ms after the DS_M peak corresponding to a SG_{sr} oscillatory frequency of 34 Hz, whereas the probability of observing a MG_{slm} oscillatory cycle is not different (20-ms window around DS_M events compared to chance: paired $t_7 = 0.79$, $p = 0.45$; Fig 4A, right). We note there is a non-oscillatory increase of the MG_{slm} oscillatory cycle probability before DS_M (50-30 ms before DS_M versus chance: paired $t_7 = 3.80$, $p = 0.007$; Fig 4A, right) and a strong reduction of the probability of observing a MG_{slm} oscillatory cycle after DS_M (30-50 ms after DS_M versus chance: paired $t_7 = 7.39$, $p = 10^{-4}$; Fig 4A, right). The patterns of SG_{sr} and MG_{slm} modulation by DS events described here are robust. While the data in Fig. 4 were acquired during the place avoidance task, the data during rest in the home cage produce similar patterns (compare to Fig. S3A).

Since DS_M are the result of synchronous MPP activation, we considered MPP manipulations to control DS_M and causally test whether DS_M promotes SG_{dom}. While chemogenetic manipulation using Ent-tTA-HM4Di mice (Fig. S4A) reduces both the excitability and synaptic response to MPP stimulation (Fig. S4B), it does not impair hippocampus-dependent place navigation (Fig. S4C) or hippocampal place cell activity (Garner et al., 2012) or change the rates of dentate spikes (Fig. S4D). Indeed, while urethane anesthesia attenuates hippocampal spiking and LFP oscillations, it does not prevent DS events (Fig. S4E). Interestingly, stimulating the MPP does not increase the rates of DS_M events in awake mice. Instead, MPP stimulation significantly

attenuates DS_L for 500 ms and DS_M for 1000 ms following stimulation (Fig. S4F) indicating that the consequences of MPP manipulations are not straightforward (Brun et al., 2002; Kanter et al., 2017; Miao et al., 2015; Schlesiger et al., 2018).

Consequently, to rigorously test the hypothesis that DS_M promotes SG_{dom}, we examine whether spontaneous variations in DS_M events could be exploited to causally determine whether DS_M promotes SG_{dom} by increasing slow gamma and/or attenuating mid-frequency gamma. We select two features of DS_M – their prominence (difference between amplitude of the DS_M maxima and either its preceding or the following minima, whichever is smaller; Fig. 4B) and a CSD source that follows DS_M (red rectangle in Fig. 4B). This CSD source might indicate increased inhibitory drive that is strongest ~10ms after DS_M, corresponds to the DG→CA1 transmission time, and localizes to the vicinity of the hippocampal fissure and CA1 *slm*, suggesting an intriguing possibility that DS_M both increases the likelihood of CA1 slow gamma oscillations but also attenuates the likelihood of CA1 mid-frequency gamma oscillations, both of which would promote SG_{dom}. Because this feature of DS_M events, the "*slm* CSD source," is only weakly correlated with DS_M prominence, accounting for only 8% of the variance (Fig. 4C, D; r^2 = 0.084, $p < 0.0001$), we used both features of the DS_M events to evaluate the causal predictions that 1) DS_M events with a large prominence will increase SG_{sr} and 2) that DS_M events with a large *slm* CSD source will decrease MG_{slm}, each promoting SG_{dom}.

DS_M events were categorized as having high prominence (10% largest events) and low prominence (10% smallest events) and the probability of observing SG_{sr} and MG_{slm} oscillatory cycles was computed in three distinct 20-ms windows, one DURING the DS_M events, centered on the peak (orange bar in Fig. 4E), the second -50 to -30 ms in the window BEFORE (green bar in Fig. 4E), and the third in the 30 to 50 ms window AFTER (purple bar in Fig. 4E). The CA1 SG_{sr} oscillatory cycles were more likely DURING ($F_{2,17}$ = 13.10, p = 0.0005, high > low = random) and AFTER ($F_{2,17}$ = 12.15, p = 0.0007, high > low = random) the high prominence DS_M

events compared to the low prominence DS_M and random events. These patterns were not observed in relation to DS_L events (Fig. S3C). Notably, when both high and low prominence DS_M events occurred, the SG_{sr} oscillatory cycles in CA1 were most probable ~10 ms after the DS_M peak, which corresponds to the DG →CA1 transmission time. In contrast, CA1 MG_{slm} oscillatory cycles were more likely BEFORE the high prominence DS_M dentate events ($F_{2,17}$ = 8.32, p = 0.004, high > low = random) and trended towards being less likely AFTER ($F_{2,17}$ = 2.73, p = 0.09). Both the high and low prominence DS_L events increased the probability of MG_{slm} oscillatory cycles during DS_L (Fig. S3D). Together these findings are consistent with the hypothesis that DS_M causally controls SG_{sr} to promote SG_{dom} in CA1.

In further support of the hypothesis that DS_M promotes SG_{dom}, complementary patterns of promoting SG_{dom} are evident when DS_M events are categorized as being the 10% with the largest and the 10% with the smallest *slm* CSD source (Fig. 4F). CA1 MG_{slm} oscillatory cycles were more likely BEFORE ($F_{2,17}$ = 9.57, p = 0.002, large > small = random), and less likely DURING ($F_{2,17}$ = 16.93, p = 0.0001, small > large = random) and AFTER ($F_{2,17}$ = 20.68, p < 0.0001, small > random > large) DS_M events with large *slm* CSD source, compared to both random and DS_M events with a small *slm* CSD source (Fig. 4F right). CA1 SG_{sr} oscillatory cycles were more likely BEFORE (Fig. 4F left; $F_{2,17}$ = 5.39, p = 0.017, small > large = random), DURING ($F_{2,17}$ = 11.42, p = 0.001, small > large > random) and AFTER ($F_{2,17}$ = 7.00, p = 0.0071, small > large > random). Taken together, these analyses confirm the causal predictions that the prominence of DS_M and the amplitude of the associated *slm* CSD source together control the two CA1 gamma oscillations to promote SG_{dom}.

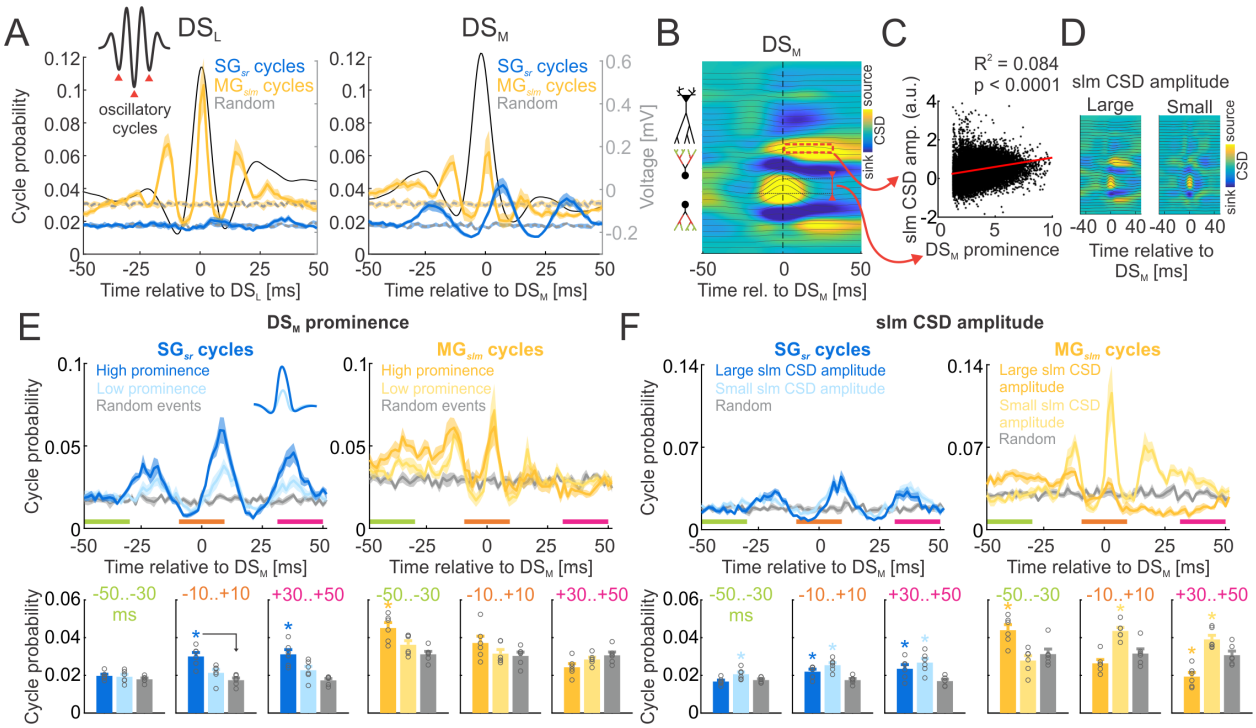

Figure 4. DS$_M$ controls the oscillatory components of SG dominance. A) Probability of oscillatory cycles (inset, red arrowheads) detected in SG$_{sr}$ (blue) and MG$_{slm}$ (yellow) relative to DS$_L$ (left), DS$_M$ (right) and random events (gray). Black lines represent average DS waveforms for reference. B) Two features of DS$_M$ that are used to assess whether DS$_M$ control the CA1 component oscillations of SG$_{dom}$ – DS$_M$ prominence (red line with reversed arrows) and the amplitude of the *slm* CSD source that follows DS$_M$ (red rectangle). C) Scatter plot of DS$_M$ prominence versus the *slm* CSD source during DS$_M$. Red line shows a linear fit to the data. D) Average DS$_M$ CSDs of the 10% of DS$_M$ events with the largest (left) and smallest (right) *slm* CSD source; the DS$_M$ prominence is similar in both plots. E) Probability of SG$_{sr}$ cycles (blue; left) and MG$_{slm}$ cycles (yellow; right) during the 10% of DS$_M$ with highest (dark color), and lowest (light color) prominence, and random events (gray). F) Probability of SG$_{sr}$ cycles (blue; left) and MG$_{slm}$ cycles (yellow; right) during the 10% of DS$_M$ with the largest (dark color), and smallest (light color) *slm* CSD source amplitude, and random events (gray). Comparisons between high/low prominence and random events (E) and large/small *slm* CSD source amplitude and

random events (F) are assessed BEFORE (-50 to -30 ms), DURING (-10 to +10 ms) and AFTER (30 to 50 ms) the DS_M events. Averages ± S.E.M. are plotted.

DS_M synchronizes DG and CA1 slow gamma band oscillations

DS_M events in dentate gyrus increase SG_{sr}, the slow gamma associated CA3 input to *sr* of CA1 to promote SG_{dom}, which begs the question of whether CA3 activity is under enhanced or reduced DG influence during DS_M? We start by studying the synchrony of CA1 and DG oscillations during DS_L and DS_M. ICA combined with CSD-based classification of DS events effectively disentangles DS events and DG oscillatory components that both originate in the perforant path projection to DG (Fig. S2D-I). ICA identified two DG components below 100 Hz (Fig. 5A; Barth et al., 2018; Fernandez-Ruiz et al., 2013). The lateral perforant path (LPP) IC (Fig. 5A, left) is associated with the outer molecular layer DG sinks in the CSD of the ICA voltage loadings and a slow gamma peak in the CA1 theta phase comodulogram (SG_{LPP}; Fig. 5A, bottom left; mean frequency 43.9 ± 5.0 Hz). The medial perforant path (MPP) IC (Fig. 5A, right) is associated with the middle molecular layer DG sinks in the CSD of the ICA voltage loadings and a mid-frequency gamma peak in the CA1 theta phase comodulogram (MG_{MPP}; Fig. 5A, bottom right; mean frequency 71.0 ± 2.7 Hz). While the mean frequency of SG_{LPP} component is higher than the mean frequency of the SG_{sr} in CA1 (paired $t_6 = 3.69$, $p = 0.01$), the mean frequency of the MG_{MPP} does not differ from the mean frequency of the MG_{slm} in CA1 (paired $t_6 = 2.17$, $p = 0.07$).

We use CA1 theta as an intrinsic network time reference and analyze the CA1 theta phase preference of the dentate SG_{LPP} and MG_{MPP} oscillations (Fig. 5B). SG_{LPP} oscillations occur at a late descending phase, close to the theta trough (277.4° ± 74.3°) that precedes both DS_M (Watson-Williams multi-sample test $F_{1,14} = 6.3$, $p = 0.03$) and SG_{sr} (Watson-Williams multi-sample test $F_{1,14} = 4.5$, $p = 0.05$). MG_{MPP} occurs close to the theta peak (214.9° ± 59.8°), similar

to DS_L (Watson-Williams multi-sample test $F_{1,14} = 1.9$, $p = 0.19$) as well as MG_{slm} oscillations (Watson-Williams multi-sample test $F_{1,14} = 0.04$, $p = 0.83$).

Because the DG SG_{LPP} and the CA1 SG_{sr} oscillations appear at similar phases of the CA1 theta cycle, and the DG MG_{MPP} and CA1 MG_{slm} also appear at similar phases of the CA1 theta cycle (Figs. 3D, 5B) an intriguing possibility exists that dentate spikes provide a means of synchronizing the DG and CA1 subfields. We test this possibility by measuring the phase coupling between the DG and CA1 slow and mid-frequency gamma IC components. We start by computing the phase locking value (PLV; Lachaux et al., 1999), a measure of the stability of the phase offset between the band-pass filtered ICs in the frequency range 20-100 Hz time-locked to DS events (Star Methods). Fig. 5C shows that the SG_{LPP} and SG_{sr} oscillations are not coupled during DS_L (Fig. 5C, top left), whereas MG_{MPP} and MG_{slm} couple during DS_L (Fig. 5C, bottom left). In contrast, the SG_{LPP} and SG_{sr} couple strongly following the DS_M peak (Fig. 5C, top right), and MG_{MPP} and MG_{slm} couple ~50 ms before and ~75 ms after DS_M (Fig. 5C, bottom right). Importantly, while PLV was computed using narrow-band filters across a wide frequency range 20-100 Hz, the phase interactions occur in relatively narrow bands, especially in the case of the DS_M-triggered events, pointing to the frequency specificity of the coupled IC components. We therefore average the PLV values across the frequency bands of interest 25-45 Hz for the slow gamma ICs and 45-85 Hz for the mid-frequency gamma ICs (Fig. 5D). To evaluate whether or not the phase coupling between the DG and CA1 gamma oscillations that are observed during DS events is simply a result of the co-occurrence of DS events and gamma oscillations at similar theta phases (Figs. 3D, 5B), we also compute the PLV around randomly selected time points that are sampled from the theta phase distributions of the DS_L and DS_M events (gray profiles in Fig. 5D). The only significant departure from randomly selected time points was during DS_M, between the SG_{LPP} and the SG_{sr} oscillations (Fig. 5D, top right; paired $t_6 = 4.04$, $p = 0.006$). The peak of this phase locking occurs 9 ms after the DS_M peak. Similarly, the

DS_M-locked SG_{sr} oscillatory cycles lag the SG_{LPP} oscillatory cycles by 6 ms (Fig. S3A, B) pointing again to the DG→CA1 transmission time that was observed in Figs. 2C and 4A.

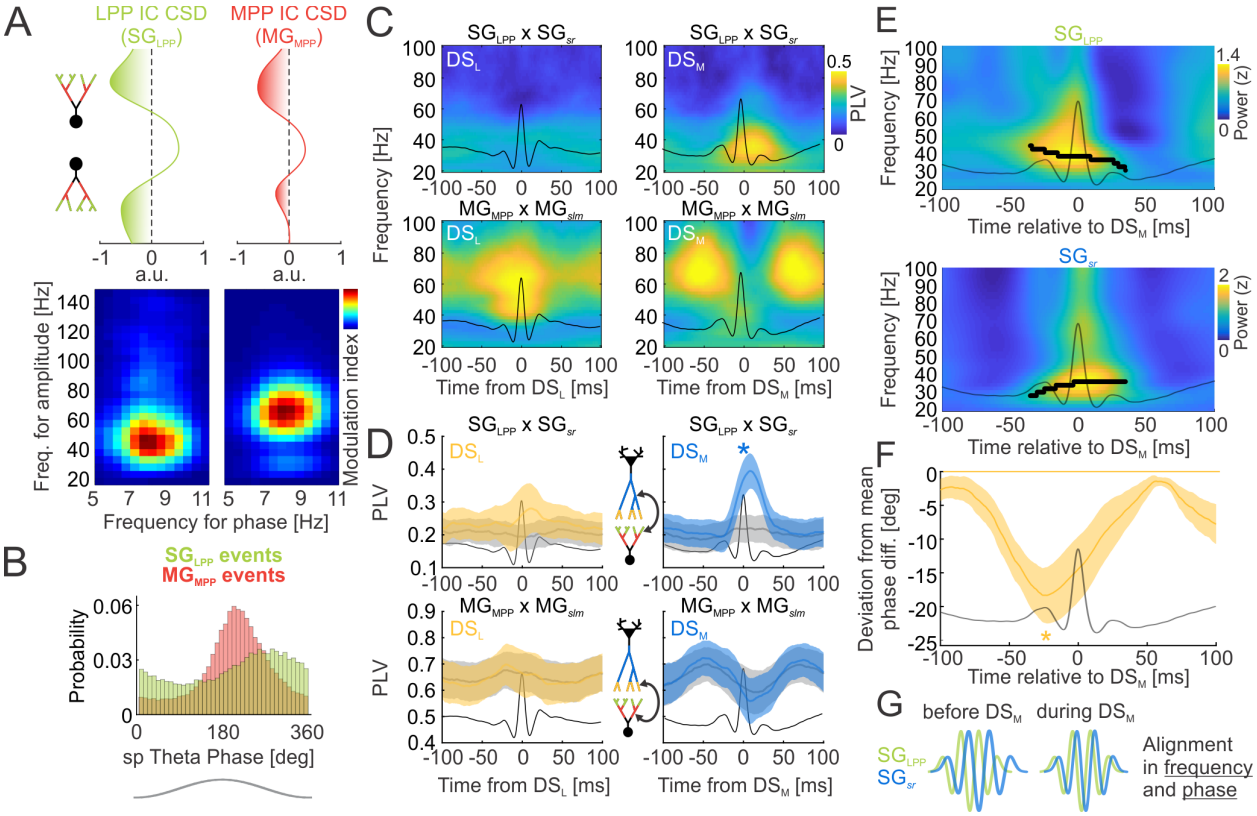

Figure 5. DS_M synchronizes the slow gamma oscillatory inputs from lateral perforant path to dentate gyrus and from CA3 to CA1 *stratum radiatum*. A) CSDs of ICA voltage loadings (top) of the LPP IC (SG_{LPP}; green), and the MPP IC (MG_{MPP}; red) in the DG. Comodulograms (bottom) between the phase of CA1 theta (5-11 Hz) and the amplitude of both IC components across 20-150 Hz show clear peaks in the slow and mid-frequency gamma range for the SG_{LPP} and the MG_{MPP}, respectively. B) Theta phase distribution of oscillatory events in the SG_{LPP} (green) and the MG_{MPP} (red). C) Example of phase locking value (PLV) between DG and CA1 slow gammas (SG_{LPP} x SG_{sr}; top) and between DG and CA1 mid-frequency gammas (MG_{MPP} MG_{slm}; bottom) time-locked to DS_L (left) and DS_M (right). Average DS_L and DS_M are in black for reference. D) Group PLV measures averaged across slow gamma (25-45 Hz for SG_{LPP} and

SG_{sr}) and mid-frequency gamma (45-85 Hz for MG_{LPP} and MG_{slm}). Gray lines are PLV profiles from random events sampled from the corresponding DS_L and DS_M theta phase distributions. Average DS_L and DS_M waveforms are in black. E) Average wavelet spectrogram of SG_{LPP} (top) and SG_{sr} (bottom) around the time of DS_M (T = 0 ms). Black dots indicate frequency of peak power at each time point ±40 ms. F) Group average of how much the instantaneous phase differences between SG_{LPP} and SG_{sr} differ from the mean phase difference. Average DS_M waveform is plotted in black for reference. Averages ± S.E.M. are plotted. G) Schematic illustration of frequency and phase alignment of SG_{LPP} and SG_{sr} during DS_M.

CA1SG_{sr} and DG SG_{LPP} are frequency- and phase-tuned during DS_M

Given a fixed duration of the gamma-generating $GABA_A$ receptor response, the frequency of a gamma oscillation can be adjusted by changing the level of network excitation, such that greater excitation produces faster oscillations because GABA inhibition can be overcome sooner (Whittington et al., 1995). Because the 44-Hz SG_{LPP} and the 34-Hz SG_{sr} oscillate at different frequencies (Figs. 3C, 5A), but phase lock during DS_M (Fig. 5D), the gamma-generating mechanism predicts input-driven changes in both the frequency and phase relationships for the phase alignment during DS_M. To test the predictions, we analyze the frequency relationships of SG_{LPP} and SG_{sr} during DS_M. The time-frequency wavelet spectrum average is computed time-locked to DS_M (Fig. 5E). Then, for each timepoint ±40 ms around DS_M we find the frequency at which the maximum power occurs (black dots in Fig. 5E). During DS_M, the frequency of SG_{LPP} decreases from 43 Hz to 36 Hz at the peak of DS_M, whereas the frequency of SG_{sr} increases from 28 Hz to 36 Hz at the peak of DS_M, effectively aligning the frequencies of the DG and CA1 originating oscillations. Next, we analyze the phase relationships of SG_{LPP} and SG_{sr} during DS_M by computing the instantaneous phase differences between the two oscillations. Because the phase differences between of SG_{LPP} and SG_{sr} vary slightly between animals, we measure the mean phase offset between SG_{LPP} and SG_{sr} for each animal independently, and then compute

the instantaneous deviation from the mean offset relative to DS_M for group statistics across animals (Fig. 5F). The maximum deviation from the mean phase difference occurs 25 ms before the DS_M peak (t_6= 4.51, p = 0.004), the phase offset reverts to the mean phase difference by 60 ms after DS_M peak (t_6= 2.37, p = 0.06). At the peak of DS_M, the phase difference is reduced by 14.5±12.8° (corresponding to a reduction from 11 to 9 ms), towards a more favorable difference for signal transmission, similar to the DG→CA1 transmission time observed in Figs. 2C, 4A, 5D and S3A.

DS_M increases DG, CA3 and CA1 discharge rates and cofiring

The findings together identify that DS_M events promote SG_{dom} (Figs. 3, 4), and synchronize oscillations activated at the LPP terminals in DG and *stratum radiatum* terminals in CA1 (Fig. 5), presumably to facilitate DG→CA1 neural transmission. The hypothesis that DS_M has a causal role in these events predicts that DS_M organizes DG, CA3, and CA1 discharge. Objectively classified, presumptive principal cells (PC) and narrow waveform interneurons (INTn) were localized and studied to test the prediction (Fig. 6A, B; Star Methods).

We compute the firing rates of presumptive granule cells (GC, n = 141), mossy cells (MC, n = 140), CA3 (n = 104) and CA1 (n = 145) principal cells as well as narrow-waveform interneurons detected in their proximity (n = 435) during 10 ms windows shifted relative to DS_L and DS_M events (Fig. 6C). These are compared with the firing rates at random times. DS events contaminated by SWR events were excluded to minimize potential SWR bias (Fig. 3G). During DS_L the discharge of GC decreases by 13% (t_{140} = 2.92, p = 0.004). Similarly, the discharge of MC decreases by 19% (t_{139} = 3.54, p = 0.0005). CA3 and CA1 principal cells did not change firing rates (Fig. 6C; CA3: t_{103} = 1.36, p = 0.18; CA1: t_{144} = 1.49, p = 0.14). In contrast, compared to baseline rates, during DS_M, GC rates increase by 106%, MC rates increase by 117%, and CA3 rates increase by 47%, whereas CA1 principal cell rates do not significantly increase as

observed during SG_{dom} (Fig. 6C; GC: $t_{140} = 5.82$, $p = 10^{-8}$; MC: $t_{139} = 6.15$, $p = 10^{-9}$; CA3: $t_{103} = 3.02$, $p = 0.003$; CA1: $t_{144} = 1.65$, $p = 0.1$). During DS_L, the discharge of GC-associated (n = 96) and MC-associated (n = 89) narrow-waveform interneurons reduces by 10% and 8%, respectively (Fig. 6C; GC INTn: $t_{95} = 2.65$, $p = 0.009$; MC INTn: $t_{88} = 2.00$, $p = 0.05$) while discharge of CA3-associated (n = 102) and CA1-associated (n = 148) narrow-waveform interneurons increases by 16% and 9%, respectively (Fig. 6C; CA3 INTn: $t_{101} = 3.72$, $p = 0.0003$; CA1 INTn: $t_{147} = 2.40$, $p = 0.017$). In contrast, during DS_M, firing rates of GC-, MC-, CA3- and CA1-associated interneurons increase by 263%, 58%, 71% and 25% respectively (Fig. 6C; GC INTn: $t_{95} = 9.51$, $p = 10^{-15}$; MC INTn: $t_{88} = 3.41$, $p = 0.0009$; CA3 INTn: $t_{101} = 6.28$, $p = 10^{-9}$; CA1 INTn: $t_{147} = 4.39$, $p = 10^{-5}$).

These findings suggest that DS_L events result in net inactivation of both excitatory and inhibitory cells in DG and weak activation of interneurons in CA3 and CA1, without changing the firing rates of CA3 and CA1 principal cells, whereas DS_M events result in strong activation of both excitatory and inhibitory cells along the DG→CA3→CA1 trisynaptic pathway, with the primary effect in CA1 being to activate presumptive interneurons. The DS_M-associated increase of both excitatory and inhibitory cells establishes the neurophysiological conditions for enhanced temporal control of principal cell discharge through the mechanisms of excitation-inhibition coordination, and enhanced opportunities for cofiring that can enhance neural transmission across the entire DG→CA3 →CA1 trisynaptic pathway (Renart et al., 2010).

Next, we analyze the cofiring of pairs of cells during DS_L, DS_M and random events by computing a peri-DS-event cofiring probability histogram for each cell pair (Fig. 6D). DS events contaminated by SWR events were excluded. Because the highest probability of observing coactive cell pairs typically occurs at the DS_M peak (Fig. 6D, bottom), we quantify each cofiring relationship by comparing the cofiring probability during the 6 ms centered at a DS peak with the

cofiring probability at random times. Each cofiring relationship is statistically evaluated using a paired t test; significance is adjusted using Bonferroni's method.

The hypothesis that DS_M promotes SG_{dom} and increased neural control via CA3, predicts increased excitatory-inhibitory co-firing during DS_M (Renart et al., 2010), as does a recent finding that the cofiring between pairs of excitatory and inhibitory cells increases in dentate gyrus during moments of active and successful discriminative memory recall (van Dijk and Fenton, 2018). Accordingly, we compare cofiring between presumptive excitatory principal cells (PCs) and inhibitory (INTn) cells within each of the GC, MC, CA3 and CA1 regions (Table S1). During DS_M, cofiring amongst the GC and associated interneuron populations increases relative to random times (Fig. 6D, left; 649 ± 734%, $t_{464} = 11.23$, $p = 10^{-26}$), whereas the cofiring decreases during DS_L (65 ± 108%, $t_{464} = 4.89$, $p = 10^{-6}$). PC and INTn cofiring within CA3 also increases during DS_M (232 ± 299%, $t_{518} = 7.18$, $p = 10^{-12}$) but does not change during DS_L (88 ± 87%; $t_{518} = 2.26$, $p = 0.02$). Increased co-firing between PC and INTn is also observed within CA1 during DS_M (132 ± 137%; $t_{361} = 5.46$, $p = 10^{-7}$) indicating potentially increased inhibitory control of principal cell spiking during DS_M events, which after Bonferroni corrections did not reach significance during DS_L (105 ± 131%; $t_{361} = 2.83$, $p = 0.005$). Consistent with this finding, we also observe strongly increased cofiring during DS_M but not DS_L between MC- and GC-associated interneurons (623 ± 676%, $t_{121} = 8.90$, $p = 10^{-15}$) and between CA3- and CA1-associated interneurons (180 ± 214%, $t_{196} = 5.53$, $p = 10^{-8}$).

These increases in the propensity for co-firing during DS_M imply that during DS_M local neurotransmission between excitatory and inhibitory cells is enhanced between monosynaptically-coupled pairs of cells. We compute spike time cross-correlograms from each simultaneously-recorded cell pair and use enhanced spike-transmission strength to identify monosynaptically-coupled cell pairs (Fig. 6E; English et al., 2017; Stark and Abeles, 2009). The matrix in Fig. 6F summarizes the types of cell-class pairs we could identify, highlighting the

greater likelihood of detecting intra-regional connectivity. The average cross-correlograms for the identified cell-class pairs confirm that during DS_M there is enhanced cofiring between excitatory – inhibitory cell pairs that are likely to be monosynaptically connected in DG, CA3 and CA1 (20 ms window; paired t test calculated at maximum cofiring value; GC/E x GC/I: DS_M: $t_3 = 3.25$, $p = 0.047$; DS_L: $t_3 = 3.07$, $p = 0.054$; CA3/E x CA3/I: DS_M: $t_{50} = 4.72$, $p = 10^{-5}$; DS_L: $t_{50} = 2.82$, $p = 0.007$; CA1/E x CA1/I: DS_M: $t_{29} = 4.32$, $p = 0.002$; DS_L: $t_{29} = 0.73$, $p = 0.47$). Furthermore, there is enhanced cofiring during DS_M but not DS_L between pairs of granule cells (GC/E x GC/E; DS_M: $t_4 = 5.43$, $p = 0.006$; DS_L: $t_4 = 0.40$, $p = 0.71$) and pairs of CA3 interneurons (CA3/I x CA3/I; DS_M: $t_8 = 2.32$, $p = 0.049$; DS_L: $t_8 = 0.29$, $p = 0.78$). Taken together, DS_M selectively activate local excitation-inhibition networks discharge in both DG and CA3, which control neuron cofiring between the DG and CA3 networks, likely to promote SG_{dom} and increased excitation-inhibition discharge in CA1.

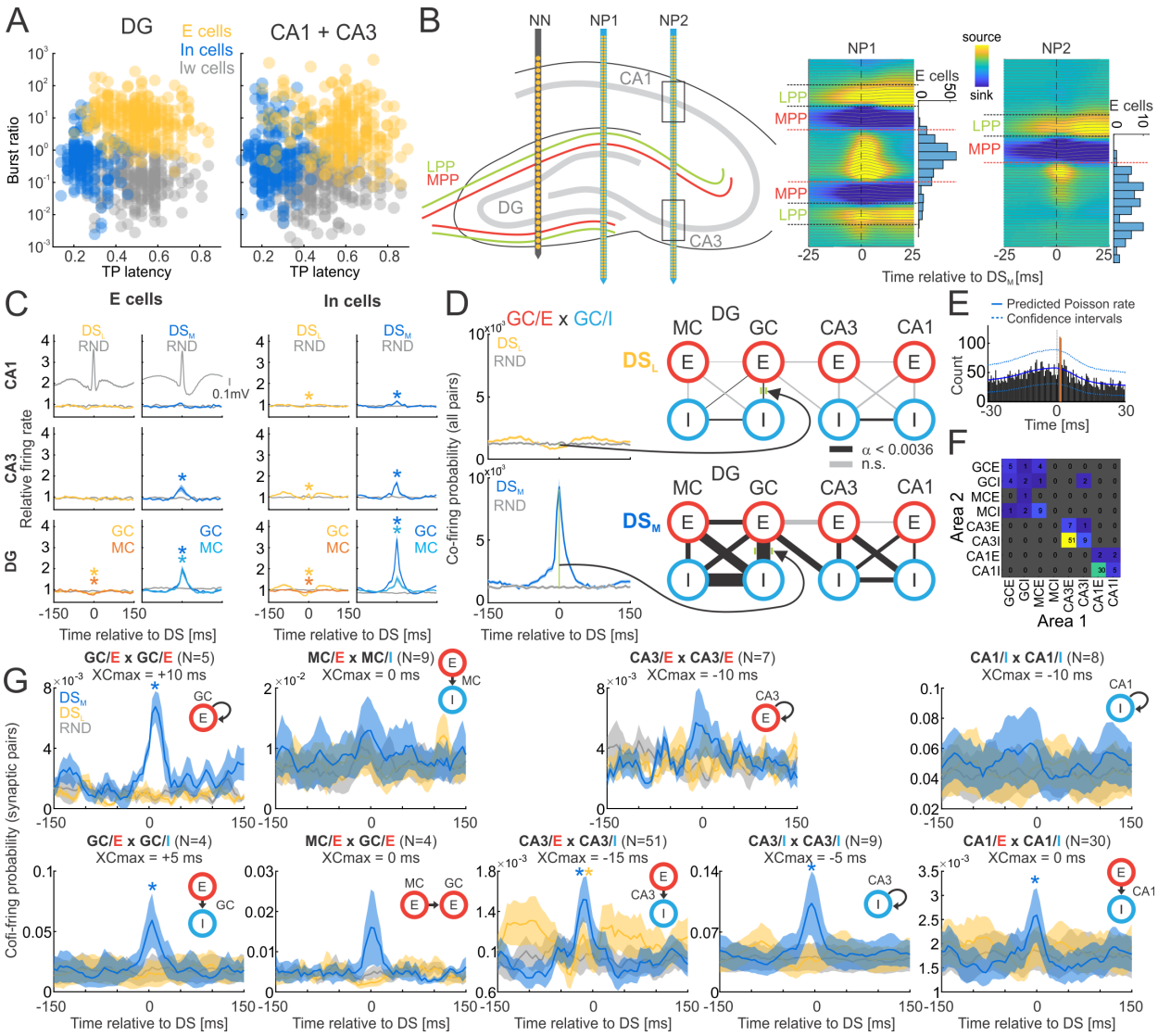

Figure 6. DS_M increases firing and cofiring in DG, CA3, and CA1 networks. A) Unitary action potentials were classified as being from excitatory cells (E), narrow-waveform interneurons (In) and wide-waveform interneurons (Iw) using the K-means algorithm on the DG-localized (left) and separately, the CA3- and CA1-localized datasets (right). B) Schematic mouse hippocampus (left) with medial placement of Neuronexus linear electrode array (NN) for detection of DS events and two example lateral placements of Neuropixel probes. NP1 represents location proximal to DG, NP2 represents location proximal to CA3. DS_M-triggered average CSDs exhibit connection asymmetry of the lateral and medial perforant paths (LPP and

MPP) that distinguishes DG and CA3 localization together with lateral placement of the electrode. Rectangles along NP2 show regions of CA1 and CA3 fields registered as isolated groups of cells (Fig. S5A). Depth distributions of putative excitatory cells from NP1 and NP2 locations are shown on the right side of CSDs. Red dotted lines represent granule cell layer, black dotted lines represent borders of outer molecular layers of DG. C) Normalized firing rates of CA1 (top), CA3 (middle), and DG (bottom) during DS_L (left) and DS_M (right) and random (gray) events. DS contaminated by SWR events were excluded, and the DS averages are shown as gray lines for reference. D) Cofiring probability of pairs of GC principal cells (GC/E) and proximal narrow waveform interneurons (GC/I) around DS_L (left, top, yellow) and DS_M (left, bottom, blue) and random (gray) events. Ratio between cofiring probability during DS events and random times is represented as line thickness (right) in a DG→CA3→CA1 network schematic; the black connections significantly differ from random times, while grey connections do not. Significance adjusted using Bonferroni's method (Table S1). E) Identification of a putative monosynaptic connection using enhanced spike-transmission strength in spike-time cross-correlogram. Solid blue line is expected cross-correlogram from Poisson model, dotted blue lines represent confidence intervals, orange bins mark significant deviations from the model. F) Summary matrix of counts of all identified monosynaptic pairs. G) Cofiring probability in identified monosynaptic pairs during DS_L (yellow), DS_M (blue) and random times (gray). Title of each subplot shows time of maximum cross-correlation relative to DS, where statistics was computed. Stars mark significant deviations from random times. Averages ± S.E.M. are plotted.

Finally, because DS_M promotes both synchronization of SG_{sr} and SG_{LPP} in the slow gamma frequency range (Figs. 5C-F), neuronal discharge (Fig. 6C) and cofiring (Figs. 6D, G) within the DG-CA3-CA1 networks, it predicts that the DS_M-enhanced SG_{sr} gamma rhythm orchestrates the discharge through spike-field coupling that can maximize the efficiency of information transfer

from DG to CA1. To evaluate this hypothesis, we examine the SG_{sr} and SG_{LPP} spike-field coupling during DS events (Fig. 7).

At the time of DS_M, the spiking of dentate granule cells, CA3 and CA1 principal cells is more organized to discharge at the trough of SG_{sr} oscillations in CA1 when compared to DS_L (Figs. 7A-C; Kuiper test comparing the DS_L and DS_M-associated discharge probability distributions across SG_{sr} phase at time T = 0 relative to DS peak; GC/E: k = 1652, p = 0.001; CA3/E: k = 465, p = 0.02; CA1/E: k = 836, p = 0.01). In contrast, at the time of DS_M, SG_{LPP} oscillations organize local spiking of dentate granule cells but not CA3 and CA1 principal cells when compared to DS_L (Figs. 7D-F; Kuiper test comparing the discharge probability distribution across SG_{LPP} phase at time T = 0 relative to DS peak; GC/E: k = 1508, p = 0.001; CA3/E: k = 374, p = 1; CA1/E: k = 516, p = 1). Similar relationships were observed for interneurons recorded in the vicinity of DG granule cells, CA3 and CA1 interneurons (Fig. S6). Taken together, these findings indicate that DS_M enhances SG_{sr}, which in turn organizes discharge across the DG-CA3-CA1 trisynaptic circuit to maximize DG-CA1 transmission and promote SG_{dom}.

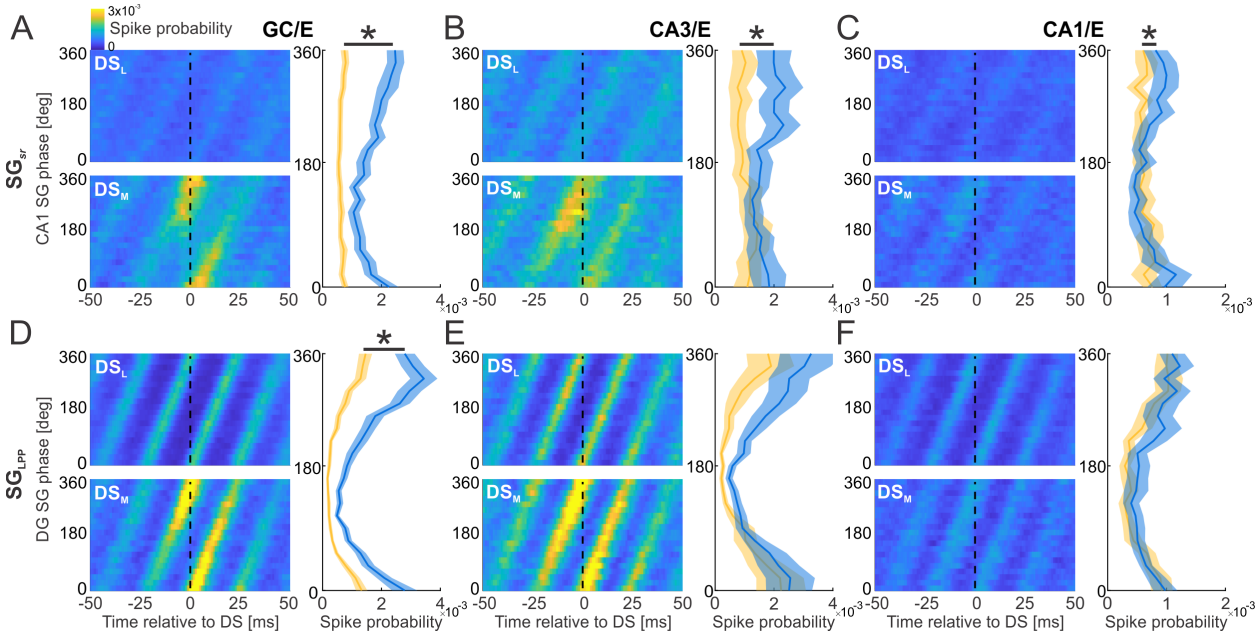

Figure 7. DS_M phase-synchronizes discharge of GC, CA3 and CA1 cells through SG_{sr} A) Average DG granule cell discharge probability relative to DS (x axis; DS_L top; DS_M bottom) and SG_{sr} phase (y axis). Group data averaged across cells for DS_L (yellow) and DS_M (blue) at DS peak (T = 0) shown on right. Stars mark a significant difference between the DS_L- and DS_M-associated phase distributions. B) Same as A, but for CA3 principal cells. C) Same as A, but for CA1 principal cells. D) Same as A, but for SG_{LPP} gamma phase (y axis) and DG granule cells. E) Same as D, but for CA3 principal cells. F) Same as D, but for CA1 principal cells.

Having identified a mechanism by which DS_M promotes SG_{dom} and increased excitation-inhibition control of CA1 discharge we examined the unintuitive prediction that during free exploration, place cells will discharge less than expected when mice walk across a cell's place field during SG_{dom}. This is because the increased discharge will preferentially represent non-local positions that do not correspond to the cell's firing field. Indeed, the standardized rate (z) of place cells during passes through the firing field is lower during SG_{dom}, than during MG_{dom} (local peaks in MG/SR ratio), and random (RND) events (Fig. S7C; $F_{2,521} = 3.16$, $p = 0.04$, $SG_{dom} < MG_{dom} = RND$) while the overdispersion of place cell discharge was similar across the three conditions (Fig. S7B; SG_{dom}: var = 4.25; MG_{dom}: var = 4.80; RND: var = 5.11; $F_{2,521} = 1.03$, $p = 0.4$), comparable to published values for mice and rats (Fenton et al., 2010; Fenton and Muller, 1998; Jackson and Redish, 2007; Talbot et al., 2018b). These findings add to the evidence that during SG_{dom}, CA1 discharge is distinct, and poorly predicted by current physical variables; this distinctive mode of hippocampus information processing is controlled by DS_M.

Discussion

Conclusion

We identify DS_M dentate spikes as a mechanism that can promote SG_{dom} events in CA1, which switch hippocampus from encoding currently experienced information to recollecting information

from the past. This is observed for example, as CA1 place cell discharge signaling the current location switching to the SG_{dom}-associated non-local CA1 discharge that signals recollected locations of shock a mouse actively avoids (Fig. 1; Dvorak et al., 2018). DS_M events at the termination zone of the medial perforant path in the dentate gyrus, control the likelihood of SG_{dom} events in CA1, and induce changes throughout Ammon's horn, consistent with the notion that DS_M events trigger a transient change in overall hippocampus function. In contrast, the consequences of DS_L events in Ammon's horn were typically, but not always, indistinguishable from baseline activity, demonstrating that the same hippocampal network can be switched into different information processing modes by synchronous population events, one of which we have identified as DS_M.

DS_M control of information processing in Ammon's horn

Our findings demonstrate extrahippocampal cortical control of information processing in hippocampus mediated by DS_M, the result of the synchronous activation of medial perforant path terminals at the middle molecular layer of dentate gyrus (Fig. 2; Bragin et al., 1995). The effects of DS_M are in dramatic and consistent contrast to the effects of DS_L, making it essential to distinguish them. In fact, conclusions based on work that did not discriminate DS_L from DS_M, have been misleading. For example, whether DS events activate or suppress dentate gyrus output to CA3 was uncertain. DS events were reported to couple to synchronous population bursts of putative hilar inhibitory interneurons and reduce multiunit CA3 and CA1 spiking (Bragin et al., 1995), suggesting that DS suppresses dentate output. This suppression was not subsequently confirmed (Flynn et al., 2015), but the idea that DS events are anti-excitatory was supported by increased DS prevalence in compensation for increased entorhinal excitation in pilocarpine-induced status epilepticus (Flynn et al., 2015). We observe that DS_L is associated with decreased discharge of DG principal cells (Fig. 6). In stark contrast, DS_M massively increased discharge of presumptive dentate principal cells and interneurons as well as CA3

principal cells, demonstrating that DS_M (but not DS_L) events result in strong dentate and CA3 activation through the EC→DG→CA3 circuit (Fig. 6). While this does not support the anti-excitatory notion, suggested by prior work that did not distinguish DS_L and DS_M, our findings are consistent with the reduced population spike latency, increased population spike amplitude, and enhanced field excitatory postsynaptic potential (fEPSP) slope that were observed during medial perforant path (MPP) stimulation triggered by undifferentiated DS events (Bramham, 1998). Indeed, we have observed that training in a place avoidance task causes synaptic plasticity of the MPP synaptic response in the suprapyramidal molecular layers of DG, and potentiation of DS_M but not DS_L, corroborating the two pathways are distinctive and can be altered independently by experience (Chung et al., preprint).

The present findings point to a process of dynamic control of hippocampal information processing marked by transient physiological events across the trisynaptic pathway. During $SG_{dom,}$ DG, CA3, and CA1 discharge is transiently elevated along with DG-CA3 cofiring (Fig. 6), and there is slow gamma frequency and phase synchronization between LPP inputs to DG and the *stratum radiatum* input from CA3 to CA1 (Figs. 5, 7), indicating involvement of the entire trisynaptic pathway, similar to SWR (Buzsaki et al., 2003; Sullivan et al., 2011). Indeed, during DS_M, SWR probability in a 20 ms window increases from 1.2% to 1.8% (Fig. 3G) and place cell discharge is non-local during SWR (Buzsaki, 2015; O'Neill et al., 2006; Papale et al., 2016; Sullivan et al., 2011) as well as during SG_{dom} (Fig. 1; Dvorak et al., 2018).

The qualitative distinction between information signaled by LEC and MEC is important in this context. LEC transmits contextual information based on objects and egocentric information that constitutes the content of spatial experience (Knierim et al., 2014; Tsao et al., 2013; Wang et al., 2018), whereas MEC transmits allocentric spatial signals like direction, distance, borders, and speed (Rowland et al., 2018; Sargolini et al., 2006; Ye et al., 2018). Remarkably, the MEC-originating DS_M signal that promotes SG_{dom} and switches CA1 to non-local positional memory

processing is coincident with synchronization between CA3-transmitted slow gamma inputs to CA1 and LEC-transmitted slow gamma inputs to DG, rather than from MEC (Figs. 5, 7). Within the “communication through coherence” hypothesis (Fries et al., 2007), the LEC→DG and CA3→CA1 inputs have a privileged opportunity for information transfer via synchronized slow gamma transmission, and so we speculate that perhaps while switching the hippocampal information processing mode, DS_M loads Ammon’s horn with information from the LEC-delivered egocentric contents of experience. In this way, during DS_M, the consequent activation of CA3 may be preferentially influenced by contextual and egocentric, ecphoric retrieval cues delivered by the LEC inputs (Kelemen and Fenton, 2013; Tulving et al., 1983). If these manifest as SG_{dom} because of the strong DS_M-associated activation of CA3 (Figs. 6, 7), the result is control of CA1 output that overrides the default control that is exerted by the mid-frequency gamma mediated ECIII input at *slm* (Brun et al., 2002). These *slm* inputs appear necessary for place cell firing (Brun et al., 2008), and they create permissive dendritic depolarization (Jarsky et al., 2005), but in principle can be shunted by the slow gamma-associated inputs (Keeley et al., 2017), and are possibly actively inhibited as a consequence of DS_M (Fig. 4F), all of which promote SG_{dom} (Fig. 3H). As we have observed during SG_{dom}, CA1 discharge will signal non-local positions that during a memory task, correspond to recollected places (Dvorak et al., 2018), and we observed here a correspondingly reduced local discharge by place cells in their firing fields (Fig. 1), despite maintained CA1 firing (Fig. 6C). Indeed, the findings of a hippocampus-wide (Figs. 6, 7), DS_M-promoted SG_{dom} control of hippocampus information processing to a non-local mode of information processing identify a source of the overdispersion that is characteristic of place cells in CA1, CA3, and DG (Fenton et al., 2010; Fenton and Muller, 1998; Hok et al., 2012; Jackson and Redish, 2007; van Dijk and Fenton, 2018), and also grid cells, although we cannot conclude the mechanism is the same (Nagele et al., 2020). The findings also offer an explanation for the possible utility of CA1 receiving two spatial inputs; the

Schaffer collaterals provide place cell inputs that can be non-local and related to mental experience, whereas the temporoammonic pathway provides an input comprised of components of place (grid cell distances, directional cells, border cells, and speed cells) more tethered to local, physical experience.

References

Barth, A.M., Domonkos, A., Fernandez-Ruiz, A., Freund, T.F., and Varga, V. (2018). Hippocampal Network Dynamics during Rearing Episodes. Cell Rep 23, 1706-1715.

Bragin, A., Jando, G., Nadasdy, Z., van Landeghem, M., and Buzsaki, G. (1995). Dentate EEG spikes and associated interneuronal population bursts in the hippocampal hilar region of the rat. J Neurophysiol 73, 1691-1705.

Bramham, C.R. (1998). Phasic boosting of medial perforant path-evoked granule cell output time-locked to spontaneous dentate EEG spikes in awake rats. J Neurophysiol 79, 2825-2832.

Brun, V.H., Leutgeb, S., Wu, H.Q., Schwarcz, R., Witter, M.P., Moser, E.I., and Moser, M.B. (2008). Impaired Spatial Representation in CA1 after Lesion of Direct Input from Entorhinal Cortex. Neuron 57, 290-302.

Brun, V.H., Otnass, M.K., Molden, S., Steffenach, H.A., Witter, M.P., Moser, M.B., and Moser, E.I. (2002). Place cells and place recognition maintained by direct entorhinal-hippocampal circuitry. Science 296, 2243-2246.

Buzsaki, G. (2015). Hippocampal sharp wave-ripple: A cognitive biomarker for episodic memory and planning. Hippocampus 25, 1073-1188.

Buzsaki, G., Buhl, D.L., Harris, K.D., Csicsvari, J., Czeh, B., and Morozov, A. (2003). Hippocampal network patterns of activity in the mouse. Neuroscience 116, 201-211.

Chung, A., Garcia-Jou, C., Dvorak, D., Hussain, N., and Fenton, A. (preprint). Learning to learn persistently modifies a cortical-hippocampal excitatory-inhibitory subcircuit. bioRxiv, 817627.

Colgin, L.L. (2015). Do slow and fast gamma rhythms correspond to distinct functional states in the hippocampal network? Brain Res 1621, 309-315.

Csicsvari, J., Hirase, H., Czurko, A., Mamiya, A., and Buzsaki, G. (1999). Fast network oscillations in the hippocampal CA1 region of the behaving rat. J Neurosci 19, RC20.

de Almeida, L., Idiart, M., and Lisman, J.E. (2009). A second function of gamma frequency oscillations: an E%-max winner-take-all mechanism selects which cells fire. J Neurosci 29, 7497-7503.

Dvorak, D., and Fenton, A.A. (2014). Toward a proper estimation of phase-amplitude coupling in neural oscillations. J Neurosci Methods 225, 42-56.

Dvorak, D., Radwan, B., Sparks, F.T., Talbot, Z.N., and Fenton, A.A. (2018). Control of recollection by slow gamma dominating mid-frequency gamma in hippocampus CA1. PLoS Biol 16, e2003354.

English, D.F., McKenzie, S., Evans, T., Kim, K., Yoon, E., and Buzsaki, G. (2017). Pyramidal Cell-Interneuron Circuit Architecture and Dynamics in Hippocampal Networks. Neuron 96, 505-520 e507.

Fenton, A.A., Lytton, W.W., Barry, J.M., Lenck-Santini, P.P., Zinyuk, L.E., Kubik, S., Bures, J., Poucet, B., Muller, R.U., and Olypher, A.V. (2010). Attention-like modulation of hippocampus place cell discharge. J Neurosci 30, 4613-4625.

Fenton, A.A., and Muller, R.U. (1998). Place cell discharge is extremely variable during individual passes of the rat through the firing field. Proc Natl Acad Sci U S A 95, 3182-3187.

Fernandez-Ruiz, A., and Herreras, O. (2013). Identifying the synaptic origin of ongoing neuronal oscillations through spatial discrimination of electric fields. Front Comput Neurosci 7, 5.

Fernandez-Ruiz, A., Munoz, S., Sancho, M., Makarova, J., Makarov, V.A., and Herreras, O. (2013). Cytoarchitectonic and dynamic origins of giant positive local field potentials in the dentate gyrus. J Neurosci 33, 15518-15532.

Fernandez-Ruiz, A., Oliva, A., Nagy, G.A., Maurer, A.P., Berenyi, A., and Buzsaki, G. (2017). Entorhinal-CA3 Dual-Input Control of Spike Timing in the Hippocampus by Theta-Gamma Coupling. Neuron 93, 1213-1226 e1215.

Flynn, S.P., Barriere, S., Scott, R.C., Lenck-Santini, P.P., and Holmes, G.L. (2015). Status Epilepticus Induced Spontaneous Dentate Gyrus Spikes: In Vivo Current Source Density Analysis. PLoS One 10, e0132630.

Fries, P., Nikolic, D., and Singer, W. (2007). The gamma cycle. Trends Neurosci 30, 309-316.

Garner, A.R., Rowland, D.C., Hwang, S.Y., Baumgaertel, K., Roth, B.L., Kentros, C., and Mayford, M. (2012). Generation of a synthetic memory trace. Science 335, 1513-1516.

Hargreaves, E.L., Rao, G., Lee, I., and Knierim, J.J. (2005). Major dissociation between medial and lateral entorhinal input to dorsal hippocampus. Science 308, 1792-1794.

Harris, K.D., Csicsvari, J., Hirase, H., Dragoi, G., and Buzsaki, G. (2003). Organization of cell assemblies in the hippocampus. Nature 424, 552-556.

Headley, D.B., Kanta, V., and Pare, D. (2017). Intra- and interregional cortical interactions related to sharp-wave ripples and dentate spikes. J Neurophysiol 117, 556-565.

Hebb, D.O. (1949). The organization of behavior, a neuropsychological theory (New York: Wiley).

Hok, V., Chah, E., Reilly, R.B., and O'Mara, S.M. (2012). Hippocampal dynamics predict interindividual cognitive differences in rats. J Neurosci 32, 3540-3551.

Hyvarinen, A. (1999). Fast and robust fixed-point algorithms for independent component analysis. IEEE Trans Neural Netw 10, 626-634.

Jackson, J., and Redish, A.D. (2007). Network dynamics of hippocampal cell-assemblies resemble multiple spatial maps within single tasks. Hippocampus 17, 1209-1229.

Jarsky, T., Roxin, A., Kath, W.L., and Spruston, N. (2005). Conditional dendritic spike propagation following distal synaptic activation of hippocampal CA1 pyramidal neurons. Nat Neurosci 8, 1667-1676.

Jia, X., Siegle, J.H., Bennett, C., Gale, S.D., Denman, D.J., Koch, C., and Olsen, S.R. (2019). High-density extracellular probes reveal dendritic backpropagation and facilitate neuron classification. J Neurophysiol 121, 1831-1847.

Jun, J.J., Steinmetz, N.A., Siegle, J.H., Denman, D.J., Bauza, M., Barbarits, B., Lee, A.K., Anastassiou, C.A., Andrei, A., Aydin, C.*, et al.* (2017). Fully integrated silicon probes for high-density recording of neural activity. Nature 551, 232-236.

Kanter, B.R., Lykken, C.M., Avesar, D., Weible, A., Dickinson, J., Dunn, B., Borgesius, N.Z., Roudi, Y., and Kentros, C.G. (2017). A Novel Mechanism for the Grid-to-Place Cell Transformation Revealed by Transgenic Depolarization of Medial Entorhinal Cortex Layer II. Neuron 93, 1480-1492 e1486.

Kay, K., Chung, J.E., Sosa, M., Schor, J.S., Karlsson, M.P., Larkin, M.C., Liu, D.F., and Frank, L.M. (2020). Constant Sub-second Cycling between Representations of Possible Futures in the Hippocampus. Cell.

Keeley, S., Fenton, A.A., and Rinzel, J. (2017). Modeling fast and slow gamma oscillations with interneurons of different subtype. J Neurophysiol 117, 950-965.

Kelemen, E., and Fenton, A.A. (2010). Dynamic grouping of hippocampal neural activity during cognitive control of two spatial frames. PLoS Biol 8, e1000403.

Kelemen, E., and Fenton, A.A. (2013). Key features of human episodic recollection in the cross-episode retrieval of rat hippocampus representations of space. PLoS Biol 11, e1001607.

Kelemen, E., and Fenton, A.A. (2016). Coordinating different representations in the hippocampus. Neurobiol Learn Mem 129, 50-59.

Knierim, J.J., Neunuebel, J.P., and Deshmukh, S.S. (2014). Functional correlates of the lateral and medial entorhinal cortex: objects, path integration and local-global reference frames. Philos Trans R Soc Lond B Biol Sci 369, 20130369.

Lachaux, J.P., Rodriguez, E., Martinerie, J., and Varela, F.J. (1999). Measuring phase synchrony in brain signals. Hum Brain Mapp 8, 194-208.

Lasztoczi, B., and Klausberger, T. (2014). Layer-Specific GABAergic Control of Distinct Gamma Oscillations in the CA1 Hippocampus. Neuron 81, 1126-1139.

Lasztoczi, B., and Klausberger, T. (2016). Hippocampal Place Cells Couple to Three Different Gamma Oscillations during Place Field Traversal. Neuron 91, 34-40.

Makarov, V.A., Makarova, J., and Herreras, O. (2010). Disentanglement of local field potential sources by independent component analysis. J Comput Neurosci 29, 445-457.

Miao, C., Cao, Q., Ito, H.T., Yamahachi, H., Witter, M.P., Moser, M.B., and Moser, E.I. (2015). Hippocampal Remapping after Partial Inactivation of the Medial Entorhinal Cortex. Neuron 88, 590-603.

Mizuseki, K., Royer, S., Diba, K., and Buzsaki, G. (2012). Activity dynamics and behavioral correlates of CA3 and CA1 hippocampal pyramidal neurons. Hippocampus 22, 1659-1680.

Nagele, J., Herz, A.V.M., and Stemmler, M.B. (2020). Untethered firing fields and intermittent silences: Why grid-cell discharge is so variable. Hippocampus n/a.

O'Neill, J., Senior, T., and Csicsvari, J. (2006). Place-selective firing of CA1 pyramidal cells during sharp wave/ripple network patterns in exploratory behavior. Neuron 49, 143-155.

Olypher, A.V., Lansky, P., and Fenton, A.A. (2002a). On the location-specific positional and extra-positional information in the discharge of rat hippocampal cells. Biosystems 67, 167-175.

Olypher, A.V., Lansky, P., and Fenton, A.A. (2002b). Properties of the extra-positional signal in hippocampal place cell discharge derived from the overdispersion in location-specific firing. Neuroscience 111, 553-566.

Pachitariu, M., Steinmetz, N., Kadir, S., Carandini, M., and Harris, K.D. (2016). Kilosort: realtime spike-sorting for extracellular electrophysiology with hundreds of channels. bioRxiv 061481 (2016).

Papale, A.E., Zielinski, M.C., Frank, L.M., Jadhav, S.P., and Redish, A.D. (2016). Interplay between Hippocampal Sharp-Wave-Ripple Events and Vicarious Trial and Error Behaviors in Decision Making. Neuron 92, 975-982.

Pastalkova, E., Itskov, V., Amarasingham, A., and Buzsaki, G. (2008). Internally generated cell assembly sequences in the rat hippocampus. Science 321, 1322-1327.

Penttonen, M., Kamondi, A., Sik, A., Acsady, L., and Buzsaki, G. (1997). Feed-forward and feed-back activation of the dentate gyrus in vivo during dentate spikes and sharp wave bursts. Hippocampus 7, 437-450.

Pettersen, K.H., Devor, A., Ulbert, I., Dale, A.M., and Einevoll, G.T. (2006). Current-source density estimation based on inversion of electrostatic forward solution: Effects of finite extent of neuronal activity and conductivity discontinuities. Journal of Neuroscience Methods 154, 116-133.

Renart, A., de la Rocha, J., Bartho, P., Hollender, L., Parga, N., Reyes, A., and Harris, K.D. (2010). The asynchronous state in cortical circuits. Science 327, 587-590.

Rolls, E.T., and Treves, A. (1998). Neural Networks and Brain Function (Oxford: Oxford University Press).

Rowland, D.C., Obenhaus, H.A., Skytoen, E.R., Zhang, Q., Kentros, C.G., Moser, E.I., and Moser, M.B. (2018). Functional properties of stellate cells in medial entorhinal cortex layer II. Elife 7.

Sargolini, F., Fyhn, M., Hafting, T., McNaughton, B.L., Witter, M.P., Moser, M.B., and Moser, E.I. (2006). Conjunctive representation of position, direction, and velocity in entorhinal cortex. Science 312, 758-762.

Schlesiger, M.I., Boublil, B.L., Hales, J.B., Leutgeb, J.K., and Leutgeb, S. (2018). Hippocampal Global Remapping Can Occur without Input from the Medial Entorhinal Cortex. Cell Rep 22, 3152-3159.

Schomburg, E.W., Anastassiou, C.A., Buzsaki, G., and Koch, C. (2012). The spiking component of oscillatory extracellular potentials in the rat hippocampus. J Neurosci 32, 11798-11811.

Schomburg, E.W., Fernandez-Ruiz, A., Mizuseki, K., Berenyi, A., Anastassiou, C.A., Koch, C., and Buzsaki, G. (2014). Theta phase segregation of input-specific gamma patterns in entorhinal-hippocampal networks. Neuron 84, 470-485.

Senzai, Y., and Buzsaki, G. (2017). Physiological Properties and Behavioral Correlates of Hippocampal Granule Cells and Mossy Cells. Neuron 93, 691-704 e695.

Stark, E., and Abeles, M. (2009). Unbiased estimation of precise temporal correlations between spike trains. J Neurosci Methods 179, 90-100.

Stella, F., Baracskay, P., O'Neill, J., and Csicsvari, J. (2019). Hippocampal Reactivation of Random Trajectories Resembling Brownian Diffusion. Neuron.

Sullivan, D., Csicsvari, J., Mizuseki, K., Montgomery, S., Diba, K., and Buzsaki, G. (2011). Relationships between hippocampal sharp waves, ripples, and fast gamma oscillation: influence of dentate and entorhinal cortical activity. J Neurosci 31, 8605-8616.

Talbot, Z.N., Sparks, F.T., Dvorak, D., Curran, B.M., Alarcon, J.M., and Fenton, A.A. (2018a). Normal CA1 Place Fields but Discoordinated Network Discharge in a Fmr1-Null Mouse Model of Fragile X Syndrome. Neuron.

Talbot, Z.N., Sparks, F.T., Dvorak, D., Curran, B.M., Alarcon, J.M., and Fenton, A.A. (2018b). Normal CA1 Place Fields but Discoordinated Network Discharge in a Fmr1-Null Mouse Model of Fragile X Syndrome. Neuron 97, 684-697.

Tort, A.B., Komorowski, R., Eichenbaum, H., and Kopell, N. (2010). Measuring phase-amplitude coupling between neuronal oscillations of different frequencies. J Neurophysiol 104, 1195-1210.

Tsao, A., Moser, M.B., and Moser, E.I. (2013). Traces of experience in the lateral entorhinal cortex. Curr Biol 23, 399-405.

Tulving, E., Le Voi, M.E., Routh, D.A., and Loftus, E. (1983). Ecphoric processes in episodic memory. Philos Trans R Soc Lond B Biol Sci 302, 361-371.

van Dijk, M.T., and Fenton, A.A. (2018). On How the Dentate Gyrus Contributes to Memory Discrimination. Neuron 98, 832-845.

Vinck, M., Oostenveld, R., van Wingerden, M., Battaglia, F., and Pennartz, C.M. (2011). An improved index of phase-synchronization for electrophysiological data in the presence of volume-conduction, noise and sample-size bias. Neuroimage 55, 1548-1565.

Wang, C., Chen, X., Lee, H., Deshmukh, S.S., Yoganarasimha, D., Savelli, F., and Knierim, J.J. (2018). Egocentric coding of external items in the lateral entorhinal cortex. Science 362, 945-949.

Whittington, M.A., Traub, R.D., and Jefferys, J.G. (1995). Synchronized oscillations in interneuron networks driven by metabotropic glutamate receptor activation. Nature 373, 612-615.

Wu, C.T., Haggerty, D., Kemere, C., and Ji, D. (2017). Hippocampal awake replay in fear memory retrieval. Nat Neurosci 20, 571-580.

Ye, J., Witter, M.P., Moser, M.B., and Moser, E.I. (2018). Entorhinal fast-spiking speed cells project to the hippocampus. Proc Natl Acad Sci U S A 115, E1627-E1636.

Zhang, K., Ginzburg, I., McNaughton, B.L., and Sejnowski, T.J. (1998). Interpreting neuronal population activity by reconstruction: unified framework with application to hippocampal place cells. J Neurophysiol 79, 1017-1044.

STAR Methods

Subjects

A total of 14 wild-type mice with a mixed C57BL6/FVB background were used for the study. The mice were 3 - 6 months old during surgery. Nine mice were implanted with linear silicon arrays. Three mice were implanted with a metal head plate for head-fixed recording using linear silicon arrays and Neuropixel probes (Jun et al., 2017). Two mice from previously published dataset were implanted with tetrodes (Dvorak et al., 2018).

Surgery

LFP recordings were collected using 32-channel (8 mice) and 16-channel (1 mouse) linear silicon array electrodes (Neuronexus, Ann Arbor, MI) with 50 μm spacing and 703 um^2 electrode area. 32-channel electrodes spanned both CA1 and DG locations, and the 16-channel electrode spanned only DG locations. The electrodes were implanted stereotaxically under isoflurane anesthesia (2%, 1 L/min). The tip was aimed at -1.85 AP, ±1.20 ML, -2.3 DV relative to bregma. The electrodes spanned the dorso-ventral axis of the dorsal hippocampus. Reference electrodes were aimed at the cerebellar white matter. The electrode assemblies were anchored to the skull using 3-4 bone screws with dental cement (Grip Cement, Dentsply, Milford DE). One anterior screw was used as a ground. A four-wire stimulating electrode bundle was made by twisting together four 75-μm diameter nichrome wires (California Fine Wire, Grover Beach, CA). The bundle was cut at an angle so as to span 0.5 mm. During surgery, the stimulating bundle was placed in the ipsilateral perforant path +0.5 AP, ±4.1 ML, 1.0-1.6 DV from lambda. Evoked response waveforms were carefully checked with different pair combinations of stimulation electrode channels. In the mice that were used for head-fixed recordings, a titanium head plate was attached to the skull using dental cement and the exposed skull was covered with KwikSil, a low toxicity adhesive (World Precision Instruments, Sarasota, FL) and protected with an

attached plastic cup. All mice were allowed at least 1 week to recover. In mice that were used for head-fixed recordings, a secondary surgery was performed immediately before the experiment. The plastic cap and KwikSil was removed and a skull opening to enable electrode placement was drilled at 1.85 AP, ±1.20 ML relative to bregma. Between consecutive days of recordings, a KwikSil protective cup assembly was reattached to prevent infection.

Behavioral tasks

9 mice with implanted linear silicon probe arrays and 2 mice implanted with tetrodes were trained in place avoidance task. Each day consisted 30 min rest session in the homecage placed in the recording chamber followed by 30 min place avoidance session. After habituation (shock off), total of 3 training sessions (shock on) were administered to all animals, one session each day, following with a retention session (shock on) 1 week after. Electrophysiology data from 9 mice implanted with linear silicon probe arrays and recorded during rest were used for Figs. 2, 3A-G and 5. Electrophysiology data from the same group recorded during place avoidance were used for Figs. 1A, B, 3H and 4. Electrophysiology data from the 2 mice implanted with tetrodes were used for Figs. 1C, D. Two mice were recorded in a custom head fixed setup utilizing both Neuropixels and Neuronexus linear silicon probe arrays during 59 sessions (average length 15.7 ± 3.9 min) spread over multiple days. Mice were encouraged to walk using custom water delivery system. Electrophysiology data recorded in head-fixed mice were used for Figs. 6, 7.

Electrophysiology recording

An amplifier board with 32 unipolar inputs and 3-axis accelerometer (RHD2132, Intan Technologies, Los Angeles, CA) was connected directly to the Neuronexus probe for signal amplification and digitization. A lightweight, counter-balanced cable (Intan Technologies, Los Angeles, CA) was used to power the amplifier board and the infrared LED used for tracking as

well as to transmit digital data to the computer using a custom recording system connected to the USB port of a PC. The cable was connected through a lightweight commutator to enable free movement of the animal. The signal from each electrode was low-pass filtered (500 Hz) and digitized at 2 kHz. Evoked responses were obtained using a constant current stimulus isolation unit (WPI, Sarasota, FL; model: A365RC) that was used to deliver individual unipolar 100 μs stimulus pulses across the electrode pair. Evoked responses were low-pass filtered at 4 kHz and sampled at 8.12 kHz. In head-fixed recordings, the signal from a Neuropixels probe was filtered between 0.5 Hz and 1 kHz and sampled at 2.5 kHz for LFP recordings and filtered between 300 Hz and 10 kHz and sampled at 30 kHz for single unit recording. Both electrophysiology systems were synchronized using square TTL pulses generated by the Neuropixels system that was recorded by both systems. The animals were recorded during a 30-minute session in their homecage during the first exposure to the experimental room. The mouse's movements during recordings was monitored continuously using a video tracking system (Tracker, Bio-Signal Group, Acton, MA) that was synchronized to the electrophysiology data using the video frame pulses generated by the camera.

Data Analysis

LFP and electrode localization

LFPs were localized by visual LFP inspection of sharp-wave ripples in CA1 *stratum pyramidale* and dentate spikes in the hilus of the dentate gyrus (Fig. S1A). Electrode locations were verified histologically at the end of recordings (Fig. S2B, C). In the mouse implanted with the 16-ch electrode array, only dentate LFPs were recorded because of the limited spatial span of the electrode.

Detection of SG_{dom} events

A published algorithm was used to extract oscillatory events from LFP or independent components obtained using ICA (Dvorak and Fenton, 2014). LFP is transformed into a time-frequency power representation by convolving the LFP/IC signal with a group of complex Morlet wavelets and z-score normalizing each band-specific signal. Oscillatory events are detected as local peaks in the normalized 2-D time-frequency space. Detection of oscillation rates and SG_{dom} events was described previously (Dvorak et al., 2018). Oscillation rates (Fig. 1A, lower) are computed as the number of detected events in a representative frequency range (30-50 for CA1 slow gamma, 70-90 Hz for CA1 mid-frequency gamma) in a 1-s window advanced by 0.25 s and smoothed using 2.5 s moving average. SG/MG ratio (Fig. 1A, lower) is computed as a ratio of CA1 slow gamma oscillation rate and CA1 mid-frequency gamma oscillation rate. SG_{dom} events, are defined as local peaks in SG/MG ratio with prominence exceeding 1 and SG/MG ratio > 1 (corresponding to SG > MG).

Detection and classification of dentate spikes

The LFP channel with the largest visually identified amplitude of dentate spike was band-pass filtered 5-100 Hz and the amplitude was z-score normalized. Next, all local peaks in the band-pass signal were detected, and several features were extracted, including the amplitude difference between the DS maxima and the preceding as well as following minima, and also the spike width that was measured at the level of either the preceding or following minima, whichever was closer to the maxima. The spike amplitude distributions were further normalized by z-score normalization of the log-transformed amplitudes. Putative dentate spikes were selected if the amplitudes compared to the preceding and following minima were > 0.75 and when the width of the event was between 5 and 25 ms. The optimal values were selected based on analysis of the feature histograms.

Dentate spikes were classified as DS_L and DS_M based on their CSD profiles (Bragin et al., 1995). CSDs were calculated using the CSDplotter Matlab toolbox (Pettersen et al., 2006) at the peak of a putative DS event. Independently for each recording, the CSD for each putative DS event was analyzed for local minima, corresponding to CSD sinks (Fig. 2B). The histogram of detected local minima of all putative DS events was plotted and the local maxima that represented the highest probability of current sinks were manually identified (color dots in Fig. 2B, middle). This analysis resulted in 4 locations corresponding to (from top to bottom) the outer and the middle molecular layers of the suprapyramidal DG blade, and the middle and the outer molecular layers of the infrapyramidal DG blade. DS_L and DS_M were then identified from the suprapyramidal DG blade as putative DS events with a sink occurring $\pm$ 25 μm around the location selected in the sink histogram, although the results did not change when classification from infrapyramidal DG blade was used instead. Putative DS events with sinks in both the outer and middle molecular layers (1.7 $\pm$ 1.5 %; mean $\pm$ S.D.) as well as with no sinks detected in either the outer or the middle molecular layers (30.5 $\pm$ 17.8 %) were excluded from analyses. Only putative DS events with exclusive sink in either the outer or the middle molecular layer (67.8 $\pm$ 18.3 %) were classified as DS_L and DS_M respectively.

Detection of ripple events

We followed a previously published algorithm (Csicsvari et al., 1999) with several modifications to detect ripple events. We used the LFP recorded from the CA1 *stratum pyramidale* electrode, where ripples were identified visually. First, the signal was 150-300 Hz band-pass filtered. Next, we computed the sliding root-mean square (RMS) estimate in a 10-ms window. Next, we z-scored normalized the RMS estimate and detected local maxima with $z > 3$. Finally, for each detected event, we computed the wavelet time-frequency representation of the LFP and for each detected event we extracted its frequency as a local peak in the time-frequency wavelet

spectrum (similar to detection of gamma oscillations described earlier). Only events with frequencies between 130-250 Hz were selected for further analysis.

Independent components analysis of the LFP

We used independent component analysis (ICA) to extract the specific CA1 dendritic components (Fernandez-Ruiz and Herreras, 2013; Fernandez-Ruiz et al., 2017), which minimizes the impact of volume conducted signals and estimates the components that can be precisely matched to specific dendritic compartments. LFP signals that were recorded using linear silicon array electrodes were decomposed into individual dendritic components using a previously described procedure (Fernandez-Ruiz and Herreras, 2013; Fernandez-Ruiz et al., 2017; Makarov et al., 2010) with several modifications. First, LFP signals were filtered between 20 Hz and 150 Hz. Next, principal component analysis (PCA) was applied to the filtered LFP data in order to find how many principal components explain over 99% of the signal variance in the data. Next, independent component analysis (ICA) was applied to the filtered LFP data using the FastICA Matlab toolbox (Hyvarinen, 1999) by specifying number of principal components that were obtained in the previous steps for both PCA-based dimensionality reduction and the target number of resulting independent components. Next, components of the unmixing matrix were used to compute CSDs of the individual voltage loadings for component localization and independent components (ICs) were processed using comodulogram analysis for frequency-based classification of components. Here, we took advantage of theta phase coupling of gamma oscillations, which can reveal a specific frequency footprint of each component (Schomburg et al., 2014). Specifically, the LFP from the *stratum pyramidale* electrode was filtered using set of FIR filters with 2 Hz bandwidth, in the range 5-11 Hz followed by the Hilbert transform to obtain the phase of CA1 theta oscillations. Next, independent components were filtered using 20 Hz wide filters in the range 20-150 Hz followed by the Hilbert transform to obtain amplitude information from individual components. Details of the filters and

filtering procedure were described previously (Dvorak and Fenton, 2014). The phase and amplitude information were then combined between all pairs of frequency bands used to obtain phase and amplitude information and a modulation index (Tort et al., 2010) was computed for each pair resulting in a comodulogram (Figs. 3C, 5A) that reveals the peak coupling between the phase of theta and the amplitude of a given IC. We found that the ICA analysis provides better segregation of the independent components if the number of LFP channels is restricted before applying ICA. On the other hand, it is not possible to say which LFP channels to include in the analysis for best IC separation. Consequently, we performed a grid search, where we systematically repeated ICA for different numbers of included contiguous segments of LFP channels referenced either to *stratum pyramidale* for CA1 (Fig. 3) or to the *hilus* for DG (Fig. 5). The resulting CSD profiles of ICs were then visually compared and selected based on both the CSD profile of voltage loadings and a clearly isolated peak of coupling between theta phase and the amplitude of a given component. While this operation is extremely computationally intensive, it allowed robust detection of the corresponding components in all the mice we studied (Fig. S2A).

Phase locking analysis

To study the phase coupling between different oscillatory rhythms, we used the phase locking value (PLV) estimate (Lachaux et al., 1999), which provides a good estimate of phase locking for signals where the volume conducted signals have been minimized by ICA (Vinck et al., 2011). To calculate PLV of a pair of signals, we used an array of complex Morlet wavelets spaced by 1Hz between 20 Hz and 100 Hz convolved with each of the ICs in the pair to obtain the instantaneous phase of both ICs at a given frequency. Next, we computed the instantaneous phase difference between the two ICs, IC_1 and IC_2. Then, for all pairs of time offsets in the range -100 ms to +100 ms relative to the DS event and each frequency, we computed instantaneous phase differences across all DS events $\Delta\varphi(t,f) = \varphi_1(t,f) - \varphi_2(t,f)$.

Finally, we computed PLV across DS events as $PLV = \frac{1}{N}\left|\sum_{n=1}^{N} exp\left(i \cdot \Delta\varphi(t,f)\right)\right|$, where i is the imaginary unit, N is number of DS events, t is the offset relative to DS event and f is frequency used to filter signal to obtain its phase. Repeating this algorithm for a range of frequencies and offsets relative to DS events generates a time-frequency PLV estimate that is centered at each type of DS (Fig. 5C).

Detection of oscillatory cycles

To detect oscillatory cycles of oscillatory bursts (Fig. 4), we started by correcting the polarity of ICs, because the polarity of individual ICs is arbitrary (Hyvarinen, 1999). Here, we took the advantage of known relationship between hippocampal gamma oscillations < 100 Hz and spectral leakage of spiking activity (Fig. S4), that can be observed > 150 Hz at *stratum pyramidale* (Dvorak and Fenton, 2014; Lasztoczi and Klausberger, 2016; Schomburg et al., 2012). We first created a set of Morlet wavelets covering 20-50 Hz for SG_{sr} or covering 60-90 Hz for MG*slm* and used them to obtain the instantaneous phase of IC components at specific frequencies. Next, we filtered the LFP from *stratum pyramidale* in the frequency range 150-250 Hz followed by a Hilbert transform to obtain the amplitude of the high frequency activity that served as a proxy for spiking activity. Next, for each IC, we created a phase-amplitude histogram of 150-250 Hz amplitude distribution relative to the phase of IC component either in the 20-50 Hz range or the 60-90 Hz range (Fig. S2B). Finally, we visually compared the resulting relationships and corrected each component so that the 150-250 Hz spiking-proxy activity was maximal at the descending phase of the SG_{sr} close to the trough and the ascending phase of MG_{slm} close to the trough (Fig. S2B). This step allowed us to reliably correct the polarity of all components from all animals in order to reliably extract local minima of oscillatory bursts. After correcting the polarity of IC components, we detected oscillatory bursts as described earlier and then found local minima in ± 50 ms window around oscillatory peak for

SG_{sr} and ± 29 ms window around oscillatory peak for MG_{slm} corresponding to 3 cycles of oscillatory activity centered at oscillatory cycle with largest amplitude (Fig. S2C). The timestamps of individual oscillatory cycles were recorded and used for later processing.

Single unit analysis

Single units were sorted using published open-source algorithm Kilosort2 (Pachitariu et al., 2016) that is optimized for Neuropixels probes and takes advantage of GPU processing to improve algorithm performance. After automated clustering of the data, we selected only units with < 20% estimated contamination rate with spikes from other neurons that were computed from the refractory period violations relative to expected. We also excluded units with non-characteristic or noisy waveforms resulting in identifying a total of 9404 single units.

The units were then localized to neocortex, CA1, DG/CA3 and thalamus using three criteria: 1) the depth of the Neuropixel probe relative to the cortical surface, 2) localization of dentate spikes in the hilus of dentate gyrus and sharp wave ripples in CA1 *stratum pyramidale* and clustering of units along the depth of the linear Neuropixel array. The clustering of units into different regions becomes apparent when we plot the depth of the maximal amplitude of the average action potential waveform for each unit along the length of the probe (Fig. S5A). The cluster of single units that overlaps with the detected location of sharp-wave ripples was classified as CA1, whereas the cluster of units that overlaps with the detected location of DS was classified as DG/CA3. The cluster of units between CA1 and the cortical surface was classified as neocortical neurons and the large amplitude units below DG/CA3 were classified as thalamic neurons. To separate CA3 from DG units, we used two additional criteria. First, we used the anatomical location, confirmed by histology, and considered CA3 units to only be from electrodes that were more lateral than +1.5 mm relative to bregma. Second, we took advantage of the asymmetric profile of the perforant path termination in DG that is apparent in the CSD

profiles of LFPs that were recorded with Neuropixel probes and triggered by DS_M events (Fig. 6B). ECII projections to the infrapyramidal molecular layers of DG terminate at the mediolateral extent at which CA3 begins, while ECII projections to the suprapyramidal molecular layers of DG continue in parallel with CA3 (Fig. 6B; Fig. S1B). Electrodes that exhibited only a dorsal current sink were classified as CA3, while electrodes that exhibited a symmetrical pair of current sinks were classified as DG. To further classify DG cells as putative granule cells (GC) and mossy cells (MC) we took advantage of two identified locations, that of the granule cell layer at the CSD reversal between the current sink in the middle molecular layer and the current source in the hilus triggered by DS_M, and that of the maximal amplitude of the average action potential of a given cell. Cells within 150 μm of the CSD reversal were classified as GC, while cells deeper than 150 μm were classified as MC (Senzai and Buzsaki, 2017). This procedure resulted in localizing 1413 cells to neocortex, 6422 neurons to thalamus, 492 cells localized to CA1, 696 cells localized to DG and 285 cells localized to CA3.

To classify units into putative excitatory and inhibitory neurons we used a similar approach as in other studies (Jia et al., 2019; Senzai and Buzsaki, 2017; Talbot et al., 2018a) and extracted several features associated with the average action potential waveshape and features associated with firing properties (Fig. S5B). Datasets were split into DG cells and CA1 + CA3 cells because features of DG action potentials were visually different from those in CA1 + CA3 (Fig. S5C). Consequently, the two datasets were independently analyzed using the k-Means algorithm implemented in JMP 14 software to identify three clusters corresponding to three types of neurons classified as principal cells (E), narrow-waveform interneurons (In) and wide-waveform interneurons (Iw). Classification of CA1+CA3 cells separately from DG cells led to best classification results into 3 selected neuronal subtypes. In the analyses that follow, we only focus on E and In cells because of their maximal separation in the feature space (Fig. 6A).

Peri-DS-event time cofiring histogram

We assessed the probability that a pair of cells would co-fire relative to the occurrence of a dentate spike by computing a cofiring probability for each cell pair. The probability was computed in a 6 ms-long window centered on the dentate spike peak. The co-firing probability was compared to randomly sampled events to obtain a ratio of co-firing change. Statistical validation was computed using a t test between the co-firing probabilities during DS events and randomly sampled times. The significance threshold was corrected using Bonferroni's method.

Statistical analyses were performed using JMP version 14 (SAS, Cary, NC) and Matlab 2019b (Mathworks, Natick, MA). Significance was accepted at $p < 0.05$. Exact p values are reported throughout.

Dentate spikes and external control of hippocampal function

Dvorak, D., Chung, A., Park E.H., Fenton, A.A.

Supplemental Information

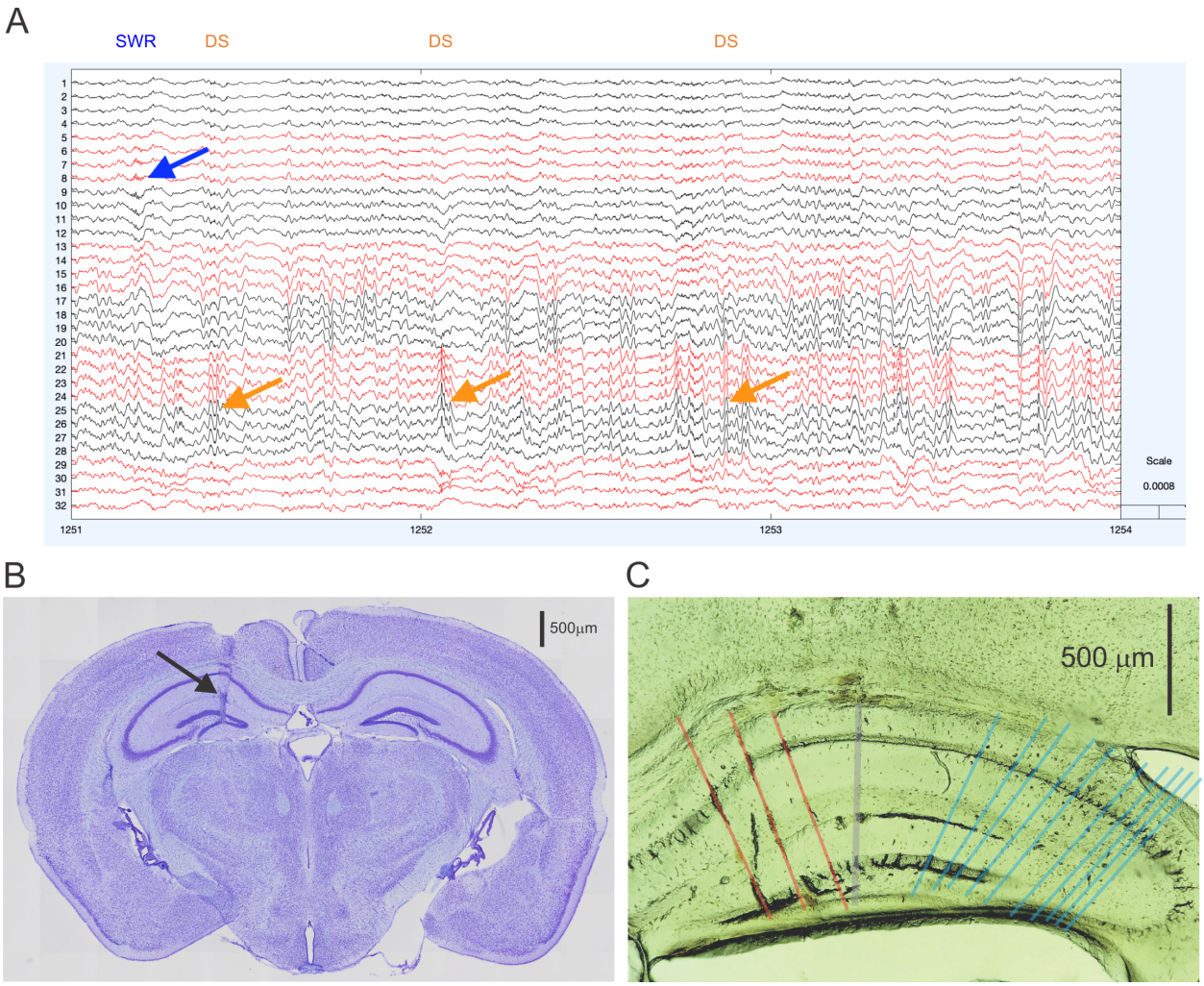

Supplemental figure S1 related to Figure 2. A) Localization of DS events (channel 25; orange arrows) and a SWR event (channel 8; blue arrow) in 3 seconds of LFP data. Scale (Volts) shown on right. B) Photomicrograph showing the trace (black arrow) of a Neuronexus 1x32 silicon probe array (6 mm shank length, 50 µm inter-site spacing, 703 μm^2 site area. C) Photomicrograph showing traces of Neuronexus probe (gray) and Neuropixel probes targeting DG (red) and CA3 (blue) using CM-DiI dye (ThermoFischer catalog V7001).

Robustness of ICA separation of DS-associated LFPs and DG gamma rhythms

Because LPP projection from LECII is an origin for both DS_L and DG slow gamma (SG_{LPP}) and because MPP projection from MECII is an origin for both DS_M and DG mid-frequency gamma (MG_{MPP}), it is theoretically possible that the DS detection and classification algorithms might be biased by strong oscillatory events (Fernandez-Ruiz et al., 2013) in the gamma range (30-100 Hz) and vice versa it is possible that DG slow gamma (SG_{LPP}) and mid-frequency gamma

(MG_{MPP}) components identified using ICA might be contaminated by DS-associated LFPs. However, this is unlikely from the following reasons. First, widths and amplitudes of detected DS events only weakly overlap with the positive hilar LFP waveforms identified at times of detected IC oscillatory events (Fig. S2D, E, F). Width and amplitude features of positive hilar LFP waveforms associated with SG_{LPP} events and DS_L overlap in 4.77% of events, SG_{LPP} and DS_M overlap in 10.38% of events, MG_{MPP} and DS_L overlap in 15.16% of events and MG_{MPP} and DS_M overlap in 17.36% of events. Those overlaps are likely further reduced after CSD-based DS_L and DS_M classification, where only DS events with precise location of CSD sinks in the outer and middle DG molecular layers respectively are selected (Fig. 2B). It should be noted that all measures were calculated from hilar LFPs at times of DS events and IC oscillatory events, because identified independent components have arbitrary amplitudes and cannot be therefore used for direct comparisons. Therefore, detected oscillatory events in DG ICs were used as timepoints to find large amplitude positive waveforms in hilar LFP and used for comparisons with DS-associated positive waveforms. Second, DS and DG IC events appear on distinct theta phases (Figs. 3D, 5B). Specifically, SG_{LPP} and DS_L that share origin in LPP projection from LECII appear at 277 and 233 degrees, respectively. Similarly, MG_{MPP} and DS_M that share origin in MPP projection from MECII appear at 214 and 344 degrees, respectively. Third, average DS and IC waveforms are clearly distinct (compare Figs. 2D and S2C). Fourth, DS-associated spectral leakage maxima (Fig. 3A) are significantly distinct from DG IC comodulogram maxima (Fig. 5A). Specifically, DS_L-associated spectral leakage maximum power appears at 50 Hz, while SG_{LPP} shows very narrow maximum at 44 Hz. Similarly, DS_M-associated spectral leakage maximum power appears at 30 Hz, while MG_{MPP} shows narrower maximum at 71 Hz. It is also theoretically possible that ICA analysis might be biased by DS events. However, this scenario is also unlikely from the following reasons. First, identified SG_{LPP} and MG_{MPP} IC components don't show positive peak time-locked to DS events in IC waveform average (Fig. S2G, H). In contrast, third identified DG IC component (DSx IC; Fig. S2I) shows multiple peaks in comodulogram and likely corresponds to DS events, especially DS_M with clear pattern of phase-synchronized low frequency component ~30 Hz corresponding to ~30Hz DS_M-associated spectral leakage (Fig. 3A) and > 100 Hz wide-band, high-frequency component, which has a likely origin in DS_M-associated increase in spiking activity (Fig. 6C; Dvorak and Fenton, 2014). Second, both DS_L and DS_M peaks are associated with SG_{LPP} oscillatory minima (Fig. S3B), and not maxima as would be the case, if IC events are biased by DS waveforms. In summary, DS events and DG IC oscillatory events can be effectively disentangled using combination of CSD and ICA analysis even though those events are associated with common hippocampal pathways.

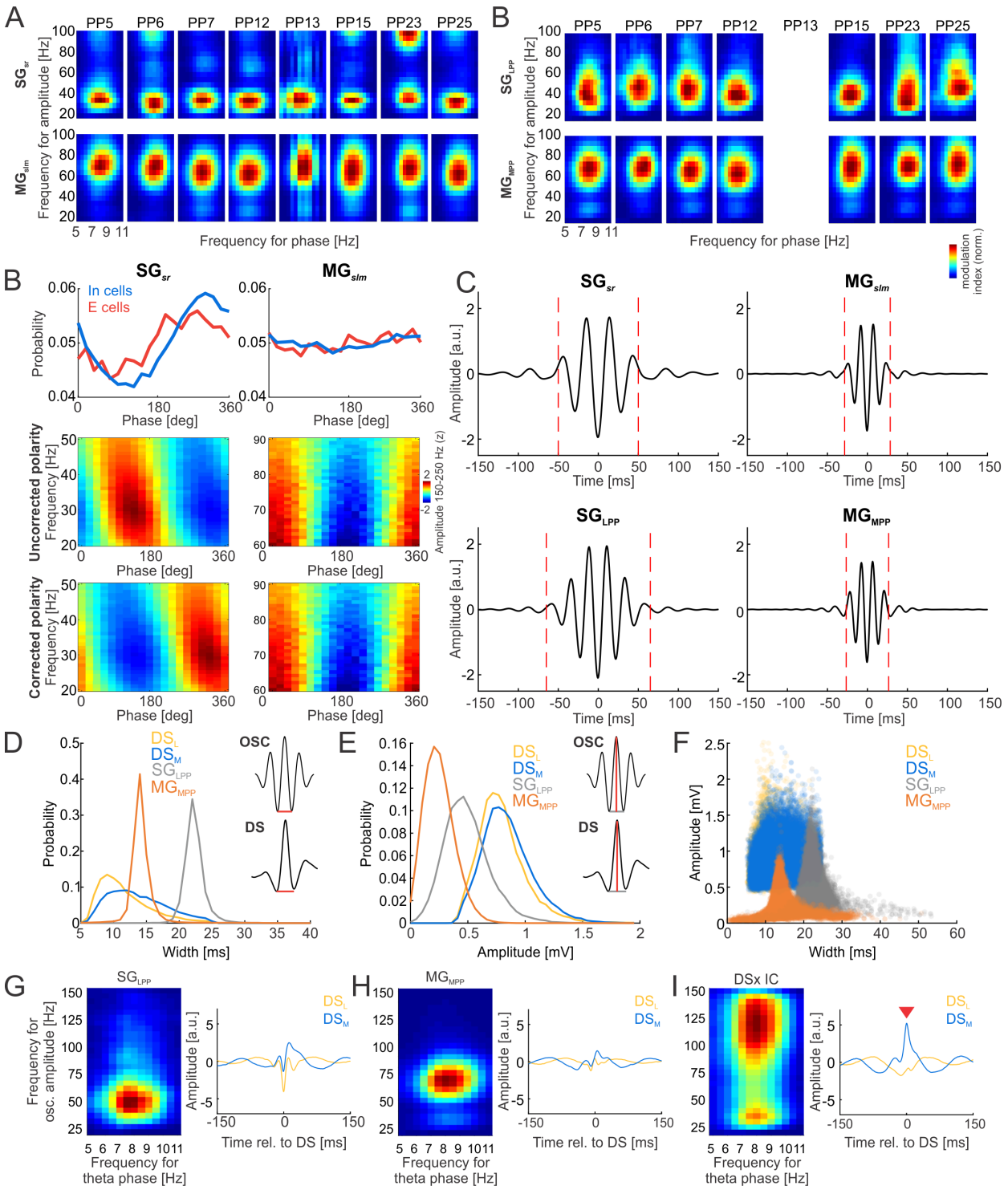

Supplemental figure S2 related to Figures 3 and 4. A) Comodulograms between LFP phase (5-11 Hz; horizontal axis) obtained from *stratum pyramidale* and amplitude of isolated independent components (20-100 Hz; vertical axis) for CA1 slow gamma (SG_{sr}; *stratum radiatum* IC; top) and CA1 mid-frequency gamma (MG_{slm}; *stratum lacunosum moleculare* IC; bottom). B) Comodulograms between LFP phase (5-11 Hz; horizontal axis) obtained from

stratum pyramidale and amplitude of isolated independent components (20-100 Hz; vertical axis) for DG slow gamma (SG_{LPP}; lateral perforant pathway IC; top) and DG mid-frequency gamma (medial perforant pathway IC; bottom). Each panel corresponds to single animal. Notice robustness of component identification across animals. B) Probability of discharge of putative CA1 excitatory cells (E, red) and inhibitory cells (In, blue) in relation to the phase of the CA1 slow gamma (SG_{sr}; top, left) CA1 mid-frequency gamma (MG_{slm}; top, right). Uncorrected CA1 slow (middle, left) and mid-frequency gamma (middle, right) phase modulation of *stratum pyramidale* high frequency (150-250 Hz) LFP amplitude selected as a proxy of spiking. Notice reversed polarity in case of SG_{sr} but correct polarity in case of MG_{slm}. Corrected polarity using component polarity inversion (bottom). Notice the alignment of discharge preference (top) and amplitude of the high frequency *stratum pyramidale* LFP (bottom). C) Average oscillatory event of CA1 slow gamma (SG_{sr}; top, left), CA1 mid-frequency gamma (MG_{slm}; top, right), DG slow gamma (SG_{LPP}; bottom, left) and DG mid-frequency gamma (MG_{MPP}; bottom, right). All oscillatory events were time-locked to local minima localized closest to the maximal oscillatory power. Oscillatory events were averaged from all animals. Red lines indicate borders of oscillatory events resulting in duration of 100 ms for SG_{sr}, 57 ms for MG_{slm}, 130 ms for SG_{LPP} and 53 ms for MG_{MPP}. Only oscillatory cycles detected within identified borders were used in analyses. D) Probability distributions of widths of positive hilar LFP waveforms identified at times of detected oscillatory events (OSC; inset) and measured between local minima preceding and following largest amplitude of DS events (DS; inset). Notice different probability distributions of DS and oscillatory events, demonstrating robustness of separation of the two classes of events. E) Probability distributions of amplitudes of positive hilar LFP waveforms identified at times of detected oscillatory events (OSC; inset) and measured as average voltage between largest amplitude and preceding and following local minima of DS events (DS; inset). Notice different probability distributions of DS and oscillatory events, again demonstrating robustness of separation of the two classes of events. F) Scatterplot of width vs. amplitude of detected DS events and amplitudes of detected positive LFP waveforms detected during oscillatory events. G) Comodulogram between the phase of *stratum pyramidale* theta LFP (5-11 Hz) and the amplitude of DG slow gamma (SG_{LPP}; left). Average SG_{LPP} waveforms locked at DS_L and DS_M events (right) show that in time of maximal positive DS amplitude (T = 0 ms), SG_{LPP} exhibits negative polarity demonstrating robustness of separation of SG_{LPP} and LFP waveforms associated with DS events. H) Comodulogram between the phase of *stratum pyramidale* theta LFP (5-11 Hz) and amplitude of DG mid-frequency gamma (MG_{MPP}; left). Average MG_{MPP} waveforms locked at DS_L and DS_M events (right) show that in time of maximal positive DS amplitude (T = 0 ms), MG_{MPP} exhibits negative polarity demonstrating robustness of separation of MG_{MPP} and LFP waveforms associated with DS events. I) Comodulogram between the phase of *stratum pyramidale* theta LFP (5-11 Hz) and amplitude of third identified IC (DSx IC), not associated with SG_{LPP} or MG_{MPP} (left). Average waveforms locked at DS_L and DS_M events (right) show that in time of maximal positive DS amplitude (T = 0 ms), DSx IC exhibits positive polarity, suggesting that DSx IC, identified independently from SG_{LPP} and MG_{MPP} components, is likely associated with DS events.

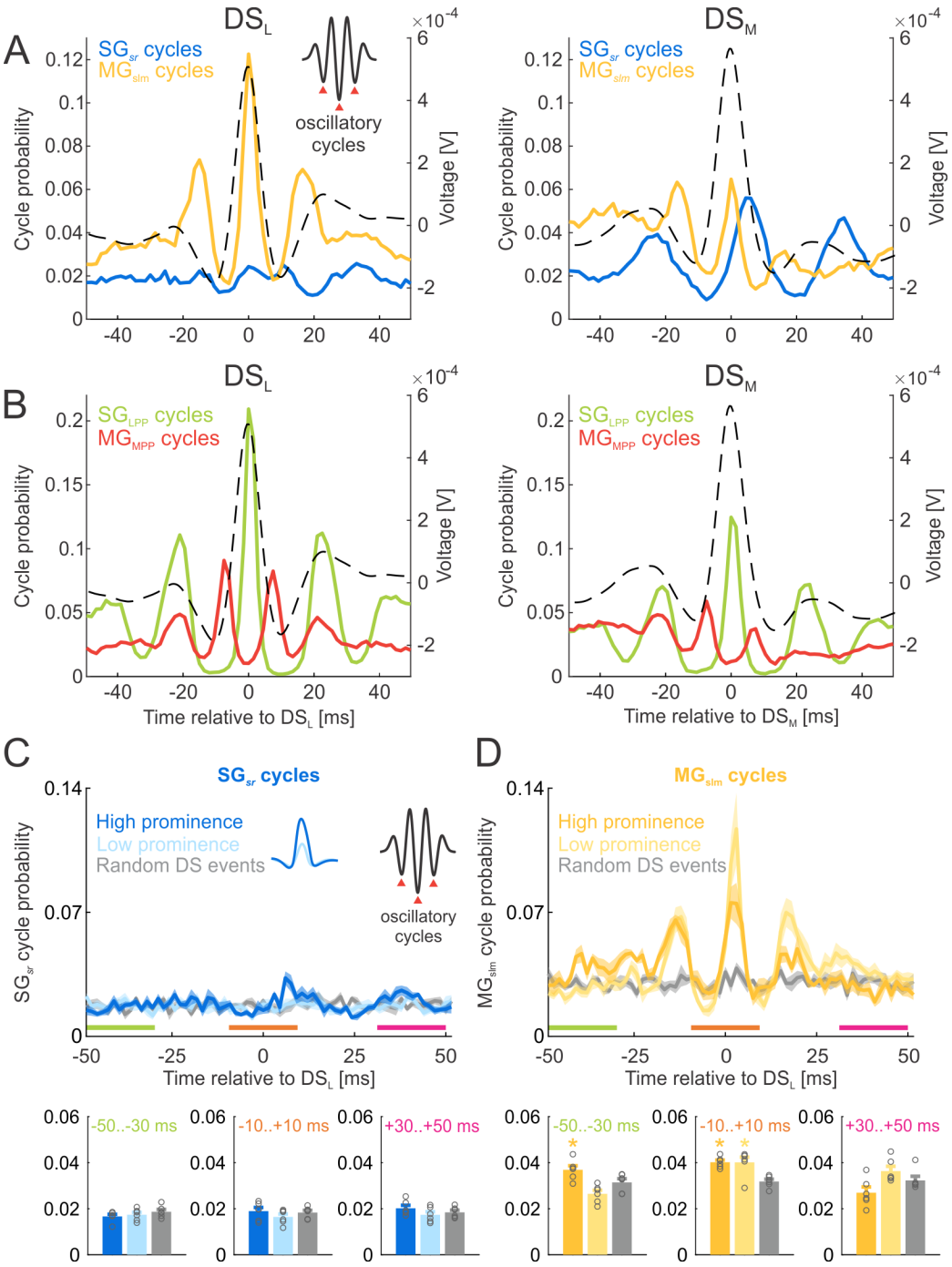

Supplemental figure S3 related to Figure 4 A) Distribution of oscillatory cycles of SG_{sr} (blue) and MG_{slm} (yellow) referenced to DS_L (left) and DS_M (right) obtained from LFPs recorded during homecage rest. Compare robustness of relationships with results obtained from LFPs during active place avoidance (Fig. 4A). DS average waveform shown as dashed line for reference. Example oscillatory events with marked oscillatory cycles (red triangles) shown as inset. B) Distribution of oscillatory cycles of SG_{LPP} (green) and MG_{MPP} (red) referenced to DS_L (left) and DS_M (right) obtained from LFPs recorded during homecage rest. DS waveform shown as dashed line for reference. C) Probability of SG_{sr} oscillatory cycles (inset) around DS_L with the 10% highest prominence (darker color) and 10% lowest prominence (lighter color). Average

probability of oscillatory cycles were assessed during -50..-30 ms before DS_L (bottom, left), -10..+10 ms centered at DS_L (bottom, middle) and +30..+50 ms after DS_L (bottom, right). No differences between high and low prominence DS_L events were observed. D) Probability of MG_{slm} oscillatory cycles around DS_L with the 10% highest prominence (darker color) and 10% lowest prominence (lighter color). Average probability of oscillatory cycles were assessed during -50..-30 ms before DS_L (bottom, left; $F_{2,17} = 12.16$; $p = 0.0007$; post-hoc tests: High > Low = Random), -10..+10 ms centered at DS_L (bottom, middle; $F_{2,17} = 16.52$; $p = 0.0002$; post-hoc tests: High = Low > Random) and +30..+50 ms after DS_L (bottom, right; $F_{2,17} = 5.74$; $p = 0.014$; High = Low = Random). Averages ± S.E.M. are plotted.

Failure to modify rates of DS events

To investigate relationship between DS events and CA1 oscillatory components, we attempted to modulate DS rates using two different methods.

First, we considered to causally decrease the rates of DS_M using chemogenetic manipulation using Designer Receptors Exclusively Activated by Designer Drugs (DREADD), specifically using a transgenic Ent-tTA mouse bred with a hM4Di-tetO mouse. The resulting mouse can be used to suppress neurons in the superficial layers of medial entorhinal cortex (MEC) that project to hippocampus through the MPP that is responsible for DS_M (Garner et al., 2012; Kanter et al., 2017). This transgenic mouse expressed the inhibitory DREADD receptor HM4Di in the MEC layers 2 and 3 (Fig. S4A). Activation of the hM4Di receptors that hyperpolarize the principal cells in superficial layers of MEC, inactivated the MPP pathway, which we confirmed using analysis of input-output curve obtained using MPP stimulation (Fig. S4B). In order to assure comparable behavioral expression, animals were trained in one-frame active place avoidance (Fig. S4C). Each session started with injection, followed by 30 min rest for drug to take effect and 30 min experiment. After pretraining (day 1, shock off, saline injection), animals were trained during 3 consecutive days (days 2-4, shock on, saline injection), followed by session with vehicle injection (day 5), CNO 10mg/kg injection (day 6), vehicle injection (day 7) and CNO 10mg/kg injection (day 8). Even though MPP was significantly attenuated (Fig. S4C), we registered no measurable effects on DS rates (Fig. S4D). These data suggest that DS generation is only weakly dependent on the MPP input, which may seem to contradict the expectations based on the effects of entorhinal lesions that were reported by Bragin in the original description of DS (Bragin et al., 1995). However, other studies focused on chemogenetic silencing of the MEC cells that contribute to the MPP confirmed almost no detectable effects, whereas chemogenetic activation caused hippocampal place cell remapping (Kanter et al., 2017). Similarly, we confirmed the ability of the dentate gyrus to generate dentate spikes even under massive reduction of neural activity under urethane anesthesia (Fig. S4E).

Second, we tried to causally increase the rates of DS_M events via electric stimulation of medial perforant path (MPP), which also gives origin to DS_M. However, this manipulation resulted in decreased DS_L rate 500 ms following stimulation (Fig. S4F, left) as well as decreased DS_M rate 500-1250 ms following stimulation (Fig. S4F, middle). Futhermore, CA1 slow gamma (SG_{sr}) power was increased while CA1 mid-frequency gamma (MG_{slm}) power was moderately decreased following stimulation, when compared to time prior stimulation (t test -1..-0.5s vs +0.5..+1s: SG_{sr}: $t_{640} = 3.8202$, $p = 0.0001$; MG_{slm}: $t_{640} = 2.3481$, $p = 0.02$). While the power CA1 gamma oscillations (SG_{sr} and MG_{slm}) changed following the stimulation, the results are inconclusive, because those changes cannot be attributed to a specific type of DS event. This is likely because both DS and their effect on hippocampal network are a result of a complex coordinated interplay between multiple classes of excitatory and inhibitory neurons as reported in previous studies (Penttonen et al., 1997) and this study as well (Fig. 6) and therefore the

electric stimulation of the perforant path creates a complex response rather than simply generating artificial dentate spikes as we hypothesized.

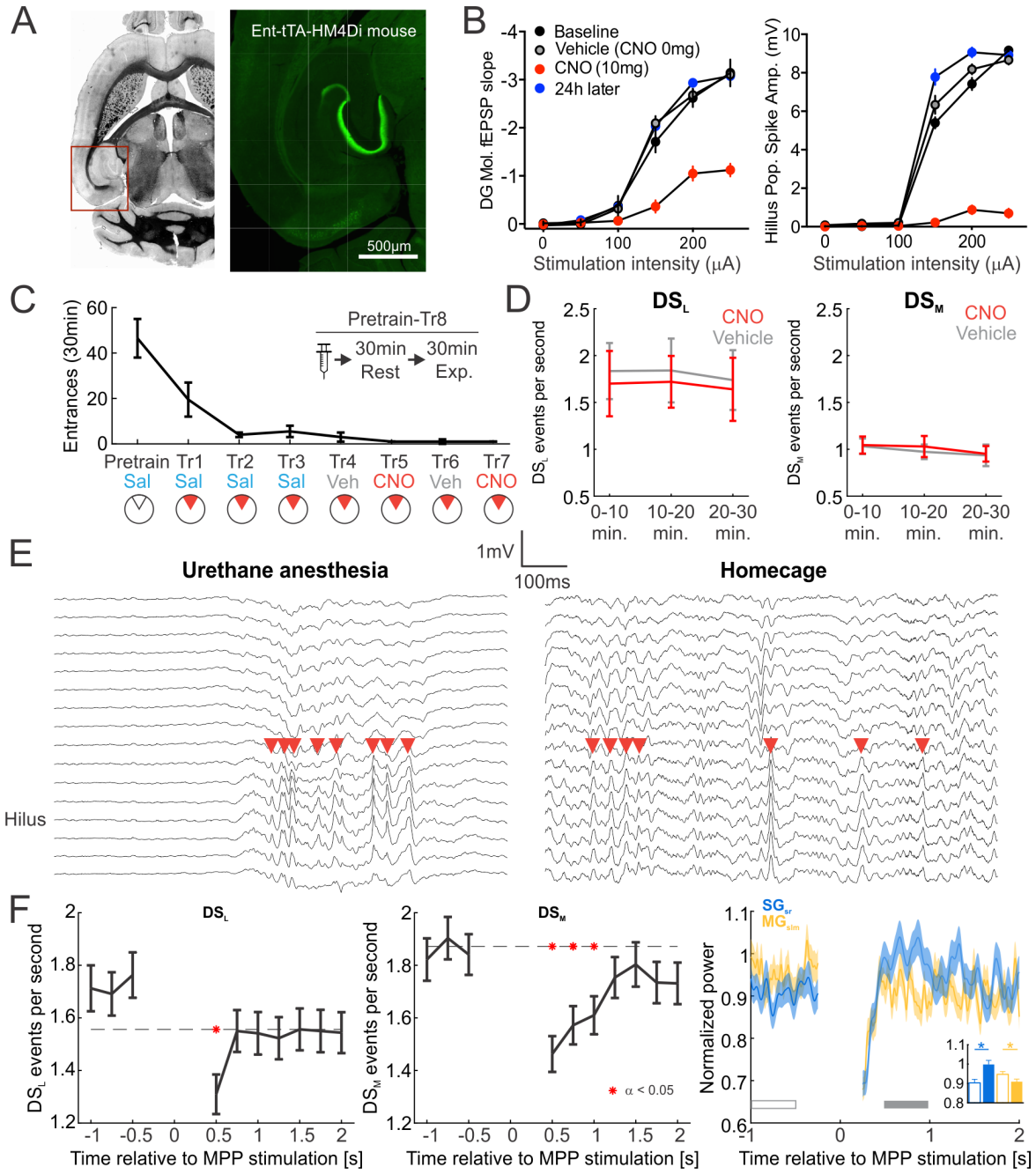

Supplemental figure S4 related to Figure 4. A) HM4Di expression in EC layer II 1 week after Doxycycline removal from the diet in Ent-tTA-HM4Di mouse. Enhanced Yellow Fluorescent Protein (EYFP) expression is confined to MEC layer II and its afferent projections to DG and CA3. B) Input-output curves illustrating that CNO activation of hM4Di causes reversible suppression of perforant path input to dentate gyrus by hM4Di activation, measured as field excitatory postsynaptic potential (fEPSP) in molecular layer of DG (left) and population spike amplitude in hilus of DG (right). C) Experimental design and behavioral performance in active

place avoidance task. D) Rates of DS_L (left) and DS_M (right) during three 10-min segments of active place avoidance. CNO shown in red, vehicle shown in gray. Data from two vehicle sessions and two CNO sessions were averaged. E) Dentate spikes (red triangles) under urethane anesthesia (left) and during rest in homecage (right). F) MPP stimulation (10 minutes off-on-off-on, 100 μs stimulus length, 15 s inter-stimulus interval, 200μA typical stimulus intensity, animal placed on a treadmill) reduces rates of DS_L (left) 500 ms following the stimulation and reduces rates of DS_M (right) 500 – 1250 ms following the stimulation. Red asterisks mark significant deviations from the mean rate.

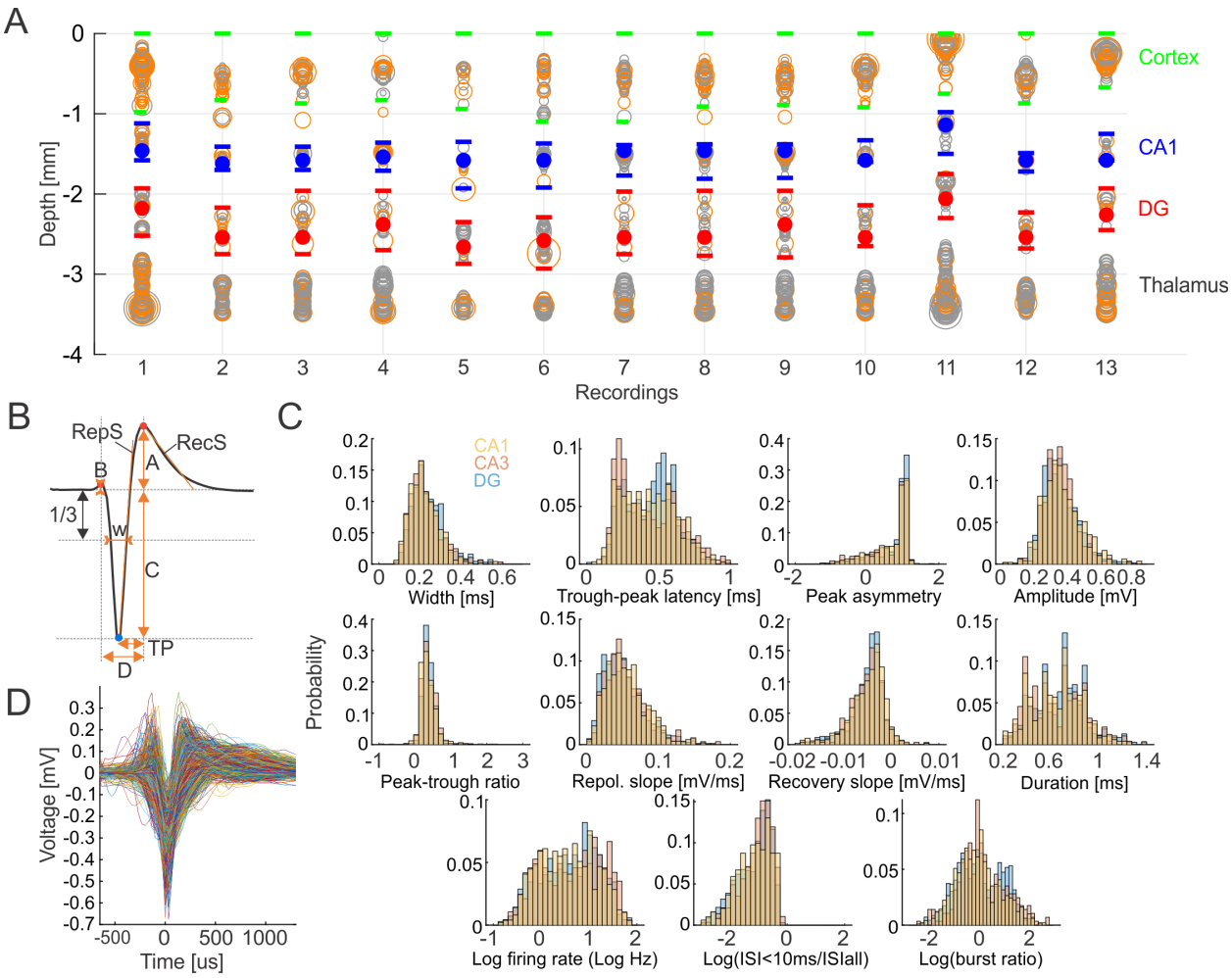

Supplemental figure S5 related to Figure 6. A) depth profile of detected single units in 13 consecutive recordings obtained using Neuropixels probes. Red dots mark depth of detected dentate spikes. Red horizontal lines mark putative DG boundary. Blue dots mark depth of detected sharp-wave ripples. Blue horizontal lines mark putative CA1 boundary. Green horizontal lines mark putative cortex boundary. B) Waveform features obtained from each isolated single unit that met the selection criteria. Width was measured as spike duration at 1/3 of spike amplitude from signal baseline (W), trough-peak latency was measured as time between spike minima and the following maxima (TP), peak asymmetry was measured as a ratio between the maximas preceding and following spike minima measured from signal baseline (b-a)/(b+a), amplitude was measured as spike amplitude with amplitude of the

following maxima (A+C), peak-trough ratio was measured as amplitude of the following maxima measured from signal baseline against amplitude of spike minima measured against signal baseline (A/C), repolarization slope was measured by fitting a regression line to the first 165 μs from spike minima towards following maxima (RepS), recovery slope was measured by fitting a regression line to the first 660 μs from the following maxima (RecS), duration was measured as time between preceding and following maximas. C) Histograms of extracted features from CA1 (yellow), CA3 (red) and DG (blue) hippocampus subfields. Notice clear bimodal distributions in trough-peak latency and Log(burst ratio) measures as wells as distinction between the features of DG and CA1+CA3 cells. D) Overlaid average waveforms of single units from CA1, CA3 and DG.

	DS_L	DS_M
GC/E x GC/I	0.65159+/-1.0831 t_{464} = -4.8941 P = 1.3649e-06	6.4937+/-7.3429 t_{464} = 11.239 P = 4.371e-26
GC/E x MC/I	0.37777+/-0.51238 t_{146} = -5.8711 P = 2.7995e-08	2.6215+/-2.5673 t_{146} = 6.1239 P = 8.0347e-09
GC/E x MC/E	0.36983+/-0.56928 t_{205} = -2.848 P = 0.0048481	2.507+/-3.2264 t_{205} = 5.9746 P = 1.0068e-08
GC/E x CA3/E	0.62202+/-0.64689 t_{54} = 0.36696 P = 0.71508	2.3396+/-1.9221 t_{54} = 2.117 P = 0.038886
GC/E x CA3/I	0.71057+/-0.70674 t_{72} = -2.0925 P = 0.039915	2.7956+/-2.2425 t_{72} = 5.6702 P = 2.7718e-07
MC/E x GC/I	0.83923+/-1.0263 t_{128} = -0.97357 P = 0.33211	4.6776+/-4.9512 t_{128} = 5.5327 P = 1.7059e-07
MC/E x MC/I	0.73545+/-0.79413 t_{113} = -1.0451 P = 0.2982	2.5696+/-2.0566 t_{113} = 5.7945 P = 6.2935e-08
MC/I x GC/I	0.83834+/-1.1095 t_{121} = -4.9891 P = 2.0546e-06	6.2324+/-6.7617 t_{121} = 8.897 P = 6.7828e-15
CA3/E x CA1/E	0.70343+/-1.0584 t_{129} = 2.05 P = 0.042394	0.74643+/-0.7919 t_{129} = 2.8737 P = 0.0047466
CA3/E x CA3/I	0.88858+/-0.87775 t_{518} = 2.265 P = 0.023926	2.3265+/-2.9999 t_{518} = 7.1865 P = 2.3315e-12
CA3/E x CA1/I	0.77526+/-0.84038 t_{224} = 0.7284 P = 0.46713	3.2339+/-4.6558 t_{224} = 3.4198 P = 0.00074447
CA3/I x CA1/E	0.8705+/-0.92127 t_{196} = -0.084586 P = 0.93268	1.8035+/-2.1411 t_{196} = 5.5339 P = 9.952e-08
CA3/I x CA1/I	1.2217+/-1.3291 t_{281} = 4.2895 P = 2.4654e-05	2.384+/-2.6306 t_{281} = 9.0801 P = 1.9735e-17
CA1/E x CA1/I	1.0562+/-1.3194 t_{361} = 2.832 P = 0.0048857	1.3288+/-1.3742 t_{361} = 5.4662 P = 8.5931e-08

Table S1 related to Figure 6D. Statistics of co-occurrence probability between two types of cells in 6 ms windows around DS_L and DS_M events compared to random times. DS events that cooccurred with SWR events were excluded from the analysis. Each 3-row entry contains a mean +/- S.D. ratio of co-occurrence probability compared to random events ($\frac{P_{DS}(cell\ type\ 1, cell\ type\ 2)}{P_{RND}(cell\ type\ 1, cell\ type\ 2)}$; first row), t test statistics (second row) and associated p-value (third row). Significant comparisons were corrected using Bonferroni's method and marked red (α = 0.0036).

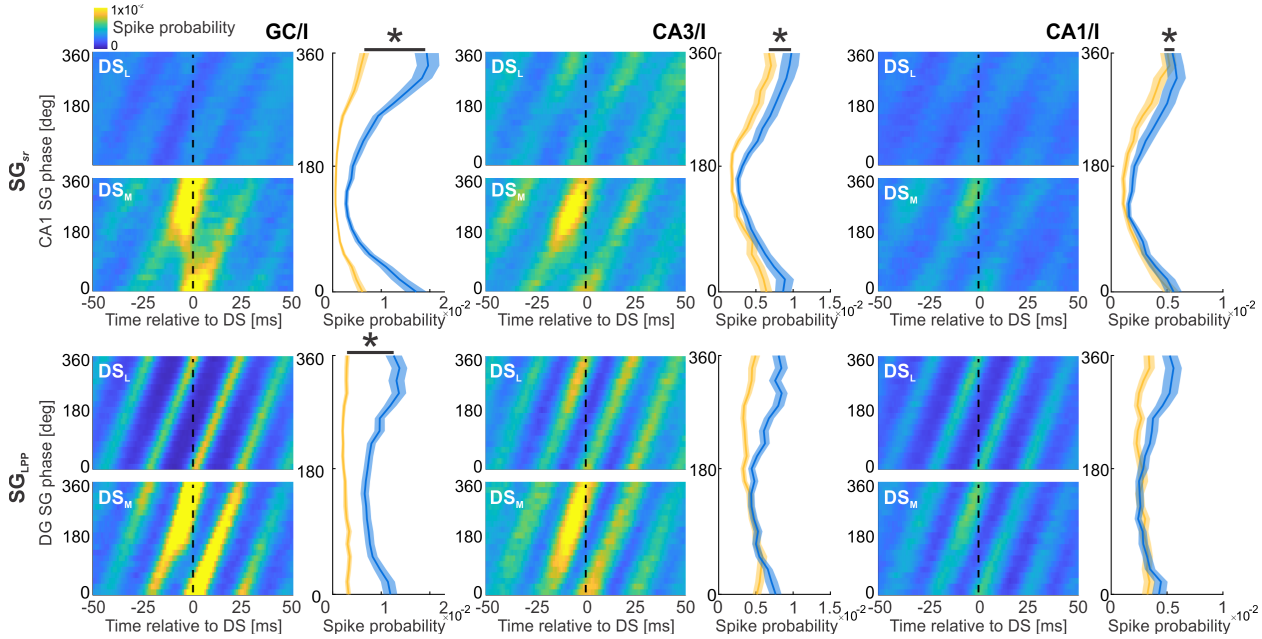

Supplemental figure S6 related to Figure 7. Discharge probability of interneurons localized in the vicinity of DG granule cells (left column), in CA3 (middle column) and CA1 (right column) relative to DS_L and DS_M events (x axis) and phase of CA1 slow gamma (SG_{sr}; top row) and DG slow gamma (SG_{LPP}; bottom row). Dashed lines marks peak amplitude of DS event, where average profiles were extracted for statistics (right side of each panel). Averages ± S.E.M. are plotted across all identified cells. Statistical comparisons performed using Kuiper two-sample test, significant differences between DS_M and DS_L marked with asterisks (SG_{sr} x GC interneurons: k = 1653, p < 0.001; SG_{sr} x CA3 interneurons: k = 2838, p < 0.001; SG_{sr} x CA1 interneurons: k = 2628, p < 0.001; SG_{LPP} x GC interneurons: k = 1160, p = 0.02; SG_{LPP} x CA3 interneurons: k = 732, p = 1; SG_{LPP} x CA1 interneurons: k = 1596, p = 0.06.

SG_{dom} promotes failures to discharge during passes through place cell firing fields

We used a previously published dataset (Talbot et al., 2018) to test a prediction of the SG_{dom}-associated recollection hypothesis (Dvorak et al., 2018) that SG_{dom} events promote failures to discharge when the mouse passes through the firing field of a place cell. We first evaluated overdispersion, the spatial discharge unreliability during passes across a place cell's firing field, using a published method (Fenton et al., 2010). Briefly, we split the recordings into 5-s long episodes and for each episode calculated the expected number of spikes as $EXP = \sum_i r_i * t_i$, where r_i is the time-averaged rate at location i, and t_i is the time spent in location i during the episode. For each 5-s interval, we then calculated z, the standard normal deviation of the observed discharge (OBS) computed under the inhomogeneous Poisson assumption as $z =$

$\frac{OBS-EXP}{\sqrt{EXP}}$. To test the prediction of the SG_{dom}-associated recollection hypothesis, for each 5-s interval we also computed the average SG/MG ratio, creating pairs of the SG/MG ratio and the standardized firing z (Fig. S7A). Large values of SG/MG correspond to SG_{dom}, and can be seen to be associated with z<0, consistent with the SG_{dom}-associated recollection hypothesis.
Next, we selected 5-s long windows centered either on detected SG_{dom} (peaks in SG/MG ratio with prominence > 1), MG_{dom} (peaks in MG/SG ratio with prominence > 1) and randomly selected events (RND) when *EXP* > the cell's average rate, as this selects passes through the cell's firing field. The variance of the distribution of the standardized firing, z describes overdispersion, the reliability of spatial firing. Overdispersion was similar across the three conditions (Fig. S7B; Var(z): SG_{dom} = 4.25; MG_{dom} = 4.80; RND = 5.11; $F_{2,521}$ = 1.03, p = 0.36), as well as to published values (Fenton et al., 2010; Fenton and Muller, 1998; Hok et al., 2013; Jackson and Redish, 2007). In contrast, as predicted, normalized firing z was lower during SG_{dom} events than the other events (Fig. S7C; ANOVA $F_{2,521}$ = 3.16, p = 0.04, SG_{dom} > MG_{dom} = RND).

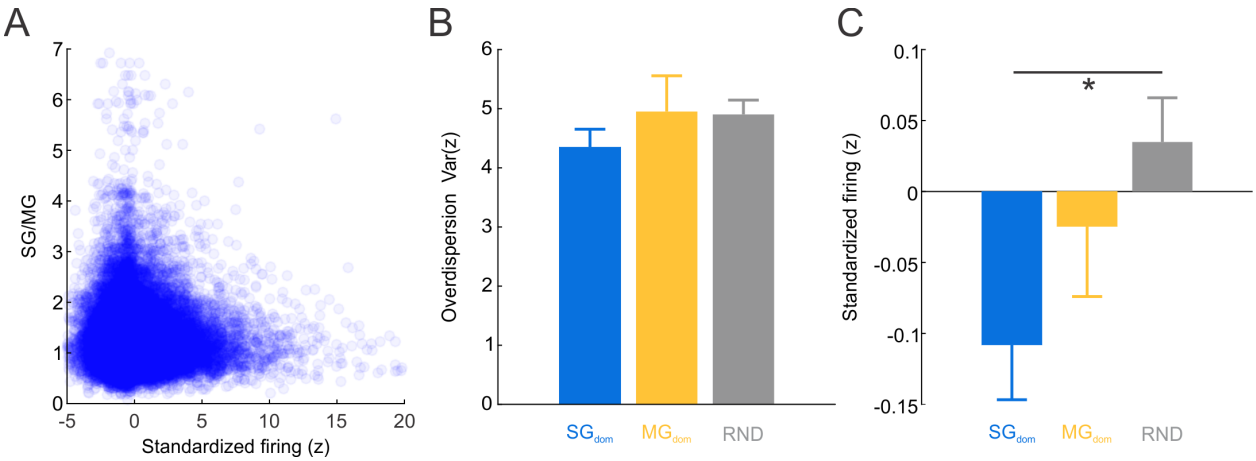

Supplemental figure S7 related to Figure 6. A) Relationship between SG/MG ratio and standardized firing (*z*). Notice lower z values during larger SG/MG corresponding to SG_{dom}. B) Overdispersion - variance of standardized firing [Var(z)] during SG_{dom}, MG_{dom} and random events. C) Standardized firing (*z*) during SG_{dom}, MG_{dom} and random events.

Summary - Relationship to Behavior

The present findings are some of the first to precisely relate DS, specifically DS_M, to overt behavior, specifically SG_{dom}-associated recollection. Impaired learning and memory was previously reported when ventral hippocampal commissure stimulation was triggered by undifferentiated DS events, according to the authors, to disrupt a hypothesized DS-associated uncoupling of the CA3-CA1 network that stabilizes memory (Nokia et al., 2017). Such results are hard to interpret, given that DS_L and DS_M affect the DG-CA1 network differentially (Fig. 3E, G, H; Fig. 4A, E, F; Fig. 5C, D; Fig. 6 C, D, G; Fig. 7A). Furthermore, DS events have different prevalence during active locomotion (Fig. 2G) that might result in stimulation during different DS types in stillness and movement. Finally, because DS_M synchronizes the precise timing of DG-CA1 network activity (Fig. 6; Fig. 7), ventral hippocampal commissure stimulation might simply disturb the precise timing required for memory encoding and recollection, resulting in impairment of learning and memory.

Supplemental References

Bragin, A., Jando, G., Nadasdy, Z., van Landeghem, M., and Buzsaki, G. (1995). Dentate EEG spikes and associated interneuronal population bursts in the hippocampal hilar region of the rat. J Neurophysiol 73, 1691-1705.
Dvorak, D., and Fenton, A.A. (2014). Toward a proper estimation of phase-amplitude coupling in neural oscillations. J Neurosci Methods 225, 42-56.
Dvorak, D., Radwan, B., Sparks, F.T., Talbot, Z.N., and Fenton, A.A. (2018). Control of recollection by slow gamma dominating mid-frequency gamma in hippocampus CA1. PLoS Biol 16, e2003354.
Fenton, A.A., Lytton, W.W., Barry, J.M., Lenck-Santini, P.P., Zinyuk, L.E., Kubik, S., Bures, J., Poucet, B., Muller, R.U., and Olypher, A.V. (2010). Attention-like modulation of hippocampus place cell discharge. J Neurosci 30, 4613-4625.
Fenton, A.A., and Muller, R.U. (1998). Place cell discharge is extremely variable during individual passes of the rat through the firing field. Proc Natl Acad Sci U S A 95, 3182-3187.
Fernandez-Ruiz, A., Munoz, S., Sancho, M., Makarova, J., Makarov, V.A., and Herreras, O. (2013). Cytoarchitectonic and dynamic origins of giant positive local field potentials in the dentate gyrus. J Neurosci 33, 15518-15532.
Garner, A.R., Rowland, D.C., Hwang, S.Y., Baumgaertel, K., Roth, B.L., Kentros, C., and Mayford, M. (2012). Generation of a synthetic memory trace. Science 335, 1513-1516.
Hok, V., Chah, E., Save, E., and Poucet, B. (2013). Prefrontal cortex focally modulates hippocampal place cell firing patterns. J Neurosci 33, 3443-3451.
Jackson, J., and Redish, A.D. (2007). Network dynamics of hippocampal cell-assemblies resemble multiple spatial maps within single tasks. Hippocampus 17, 1209-1229.
Kanter, B.R., Lykken, C.M., Avesar, D., Weible, A., Dickinson, J., Dunn, B., Borgesius, N.Z., Roudi, Y., and Kentros, C.G. (2017). A Novel Mechanism for the Grid-to-Place Cell Transformation Revealed by Transgenic Depolarization of Medial Entorhinal Cortex Layer II. Neuron 93, 1480-1492 e1486.
Nokia, M.S., Gureviciene, I., Waselius, T., Tanila, H., and Penttonen, M. (2017). Hippocampal electrical stimulation disrupts associative learning when targeted at dentate spikes. J Physiol 595, 4961-4971.
Penttonen, M., Kamondi, A., Sik, A., Acsady, L., and Buzsaki, G. (1997). Feed-forward and feed-back activation of the dentate gyrus in vivo during dentate spikes and sharp wave bursts. Hippocampus 7, 437-450.
Talbot, Z.N., Sparks, F.T., Dvorak, D., Curran, B.M., Alarcon, J.M., and Fenton, A.A. (2018). Normal CA1 Place Fields but Discoordinated Network Discharge in a Fmr1-Null Mouse Model of Fragile X Syndrome. Neuron.